Acta Materialia 208 (2021) 116716

Contents lists available at ScienceDirect

Acta Materialia

journal homepage: www.elsevier.com/locate/actamat

Strain-sensitive topological evolution of twin interfaces

Ahmed Sameer Khan Mohammed, Huseyin Sehitoglu*

Department of Mechanical Science and Engineering, University of Illinois at Urbana-Champaign, 105 S. Mathews Ave., Urbana, IL 61801, USA

ARTICLE INFO

Article history:
Received 22 December 2020
Revised 1 February 2021
Accepted 2 February 2021
Available online 7 February 2021

Keywords:
Twin boundaries
Type II twinning
Topological models
Shape memory alloys
Functional interfaces

ABSTRACT

Twin Boundaries (TBs) are fundamental interfaces in materials science which, despite over a century of research, continue to surprise us. A longstanding anomaly in the field is the experimental observation of a Type II TB in NiTi with two distinct indicial identities: $(0.7205\ 1\ \bar{1}) \approx (34\bar{4})$ and $(89\bar{9})$. The nanostructure of this interface is still unclear, with varying propositions put forth over the past 4 decades. We consider multi-scale energetics, employing Molecular Statics simulations and anisotropic elasticity formalisms, to establish a Terrace-Disconnection (TD) topology as the energy-minimal nanostructure. A theoretical framework is developed based on continuum strain-energy arguments to determine the influence of microstructural strain and local twin volume fraction on interface topology. It is shown that it is energetically favorable for the topology to evolve across a continuous spectrum of indicial identities under coupled influence of both parameters. Consequently, experimental observations that were thus far considered contrasting are proposed as distinct states within this spectrum, transposing as evidence of the proposed evolving capability in the Type II TB. This topological evolution fundamentally arises from a strain-mediated change of the dislocation-spacing (equivalently, a change in the interface dislocation-density). We further propose the prevalence of this evolving behavior in both Type I and Compound TBs (in NiTi) exhibiting a seamless transition between coherent and semi-coherent states, significantly changing dislocation-densities (upto 8-fold) and exhibiting irrational Miller-index identities under non-zero strain. An "Evolving Interface" theory is proposed as an extension to the Topological Modeling framework, allowing determination of equilibrium topologies at non-zero strain and unsymmetric twin volume fractions.

1. Introduction

Crystalline materials majorly constitute the technologically important structural and functional materials of today. The phenomenon of twinning is ubiquitous in this material class encompassing metals [1-4], ceramics [5], and minerals [6-8]. The boundaries of twins or Twin Boundaries (TBs) have long been one of the most well-researched crystalline interfaces, serving as a logical starting point to understand other complex interfaces such as grain boundaries, or phase-transformation fronts. Their presence plays an active role in dictating material strength (capable of raising it 4–5 times [9]), fracture-resistance [10], fatigue-resistance (possibly doubling it [11]) and functional performance [12-14]. Inevitably, this dictates performance in applications spanning multiple domains (e.g. biomedical devices [15], energy-harvesting [16], aeronautics, and space exploration [17]) across multiple scales of operation (from micro-scale actuators to macro-scale strengthening).

The predominant class of twins in structural and functional materials are twins formed by deformation [1,4,18], hence named "deformation twins". These twins form by shear and migrate through diffusionless dislocation-mediated mechanisms [4,19,20]. The classical theory of deformation twinning [21] established types of deformation twins based on symmetry relations between the matrix and the twin phases. There are three dominant (also called "classical") modes, namely:

1 Type I twins: The twin lattice is a reflection of the matrix lattice with the twin boundary K_1 as the mirror plane of symmetry
2 Type II twins: The twin lattice is obtained by a 180-degree rotation of the matrix lattice about the direction of twinning η_1
3 Compound twins: The twin lattice exhibits both symmetry relations above

It is worth mentioning that in cubic structures (FCC, BCC etc.) the only types of twins are compound twins [22]. All three modes will be considered in the present study. Of these classes, the best understood twinning systems are Type I and Compound twins. This is primarily because their TBs are crystallographic planes with ra-

* Corresponding author.
E-mail address: huseyin@illinois.edu (H. Sehitoglu).

https://doi.org/10.1016/j.actamat.2021.116716
1359-6454/

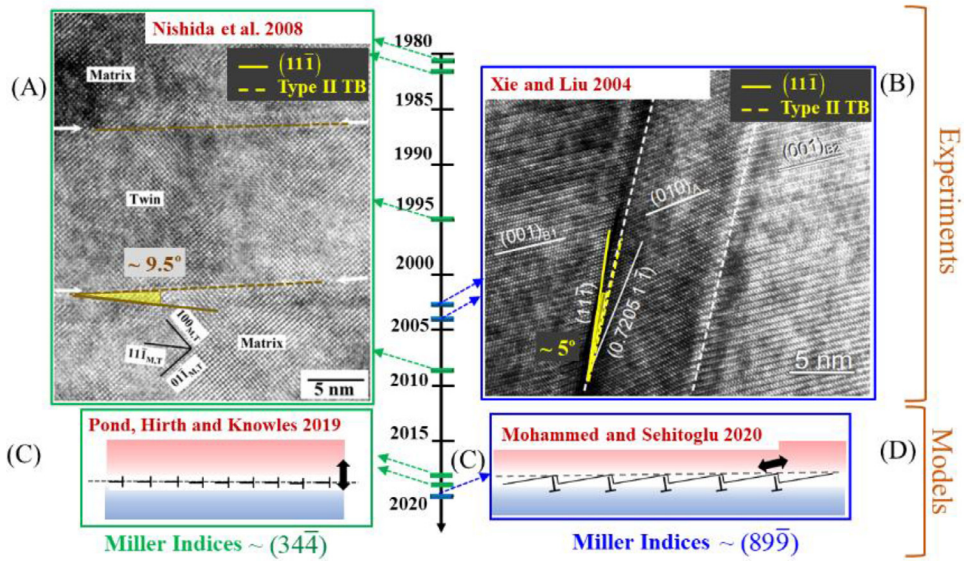

Fig. 1. A debate over three indices across four decades: (a) Experimental evidence from [42] proposing indicial identity as (0.7205 1 $\bar{1}$) ≈ (34$\bar{4}$). (b) Contrasting experimental evidence from [38] proposing the interface to be closer to (89$\bar{9}$), exhibiting a trace distinct from (0.7205 1 $\bar{1}$). (c) Tilt-Wall (T-W) interface model corroborating the suggested identity in (a); the dislocations reside on consecutive (011) planes nearly normal to the interface. (d) Terrace-Disconnection (T-D) model corroborating proposed identity in (b); the terraces are (11$\bar{1}$) planes separated by periodically spaced dislocations/disconnections (In (c, d), dashed line represents the effective interface and double-arrow represents the direction of dislocation glide; blue/green arrows indicate the time of other experimental/analytical research [23,25,26,39-41] corroborating one of the two interface nanostructures). (For interpretation of the references to colour in this figure legend, the reader is referred to the web version of this article.)

tional Miller indices. There is little to no debate surrounding the structure/topology of the TB. On the contrary, there is considerable debate around understanding of Type II TBs and a consensus on its nanostructure is yet to be reached [23-26]. This is primarily because the TBs have irrational Miller indices and seem to be of a non-crystallographic nature. It is of high importance to gain a complete understanding of Type II TBs as they play a significant role in the mechanical response of several successful functional materials e.g. NiTi [13,27-30], NiMnGa [24,31-35], CuZnAl [36] etc.

The interface which best exemplifies these challenges in understanding Type II TBs is the ⟨011⟩ Type II TB in NiTi, an important Shape Memory Alloys (SMA). The classical theory [21] analytically determines the twin plane to be of identity (0.7205 1 $\bar{1}$), a close rational approximant of which is (34$\bar{4}$). Upon experimental discovery [37], the TB closely confirmed this identity, subtending an angle around 10° with the (11$\bar{1}$) plane. It must be noted that the exact indices of the irrational interface (i.e. the exact irrational index value) cannot be fully experimentally determined. Instead, the evidence provides a close confirmation of the theoretically proposed identity of (0.7205 1 $\bar{1}$) ≈ (34$\bar{4}$). It was not until about 20 years later that contrasting evidence was put forth where the indices were proposed to be around (89$\bar{9}$) [38]. The latter observed interface subtends a much lower angle, about 5°. We note a similar disagreement in experimental results across multiple studies of the time [39-42], summarized in Fig. 1. We clarify that the quoted TEM micrographs in Fig. 1 are only representative results from the cited experimental studies [38,42] where the contrasting identities have been observed and proposed. These quoted micrographs are not the sole basis behind the concluded identities of the interface and the reader is referred to the respective experimental studies [38,42] (also others [37-41]) for a more detailed exposition. In parallel with these studies, an advanced theory of interfaces known as Topological Modeling had evolved [43]. To add to the debate, two contrasting topological models currently exist for this interface: (i) a Terrace-Disconnection (T-D) model reproducing indices (89$\bar{9}$) (Fig. 1(c)), recently proposed by the authors [26] and (ii) a Tilt-Wall model (T-W) (Fig. 1(d)) reproducing the indices (0.7205 1 $\bar{1}$) [25]. At present, after nearly 4 decades, a consensus on the nanostructure is yet to be reached.

The present study first addresses this debate and compares both proposed nanostructures based on energies on two scales: meso–scale continuum strain-energies and sub-nano-scale atomistic potential energies. The anisotropic Eshelby-Stroh formalism [44] is employed for continuum calculations and Molecular Statics is employed within the LAMMPS [45] framework for atomistic simulations. It will be shown that one of the nanostructures is energy-minimal and will be proposed as the preferred Type II TB structure. Subsequently, an "Evolving Interface" theory is developed within a linear-elastic framework emphasizing that it is energetically favorable for the proposed nanostructure to evolve depending on microstructural strain and local twin volume fraction. Consequently, we stake that the experimental observations that establish competing interface identities are in fact observations of the same nanostructure at different evolved states. The proposed evolving behavior is extended to (11$\bar{1}$) Type I and (001) Compound TBs in NiTi [46], proposing its prevalence in all major deformation twin modes.

2. Modeling methodology and results

The modeling methodology is presented concurrently with the results. The first two sub-sections are focused on evaluating the atomistic potential energy and continuum strain energy of both Type II nanostructural models proposed till date (refer Fig. 1). The final sub-section outlines the theory used to predict the evolution/change in nanostructure in response to external strain, for changing twin volume fractions. This theory will be used to explain the experimental observations of the ⟨011⟩ Type II TB in NiTi. It is further applied to the Type I and Compound TBs (specifically {111} Type I and {001} Compound TB in NiTi) to show general applicability to deformation TBs.

2.1. Evaluation of atomistic potential energies for both Tilt-Wall (T-W) and Terrace-Disconnection (T-D) nanostructures

We first evaluate potential energies on a sub-nano scale where continuum methods do not apply. The atomic structures were constructed and equilibriated using a Molecular Statics (MS) approach

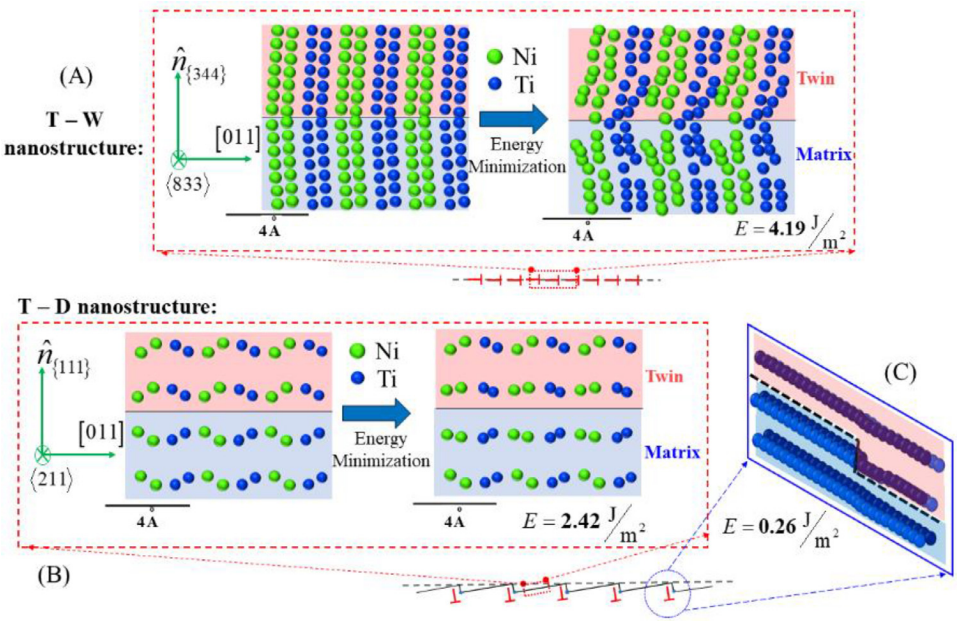

Fig. 2. Determining atomistic potential energies of T-W and T-D topologies: (a) Atomic structure of the T-W topology showing the as-constructed (unrelaxed) and energy-minimized (relaxed) structures. (b) Atomic structure of the T-D topology showing the as-constructed (unrelaxed) and energy-minimized (relaxed) {111}terrace structure and (c) atomic structure of a disconnection on the T-D nanostructure (only showing Ti atoms which are color-coded to emphasize the location of the disconnection, refer [13] for more details).

in LAMMPS [45], utilizing an interatomic potential developed in the authors' group [47]. The potential is capable of reproducing cohesive energies of multiple phases of NiTi (B2, B19, B19′) close to that predicted by ab initio Density Functional Theory (DFT) [47], and is preferred for the study. First, the atomistic evaluation of the T-W is considered. The atomic structure can be constructed by positioning the crystals of the two twin variants to meet on the $(34\bar{4})$plane, which is a close rational approximant to the irrational $(0.7205\ 1\ \bar{1})$ plane. The tilt misorientation between the two crystals is introduced by way of construction in their respective orientations [48]. The lattice constants and motif positions of atoms inside the unit cell are picked consistent with the interatomic potential [47]. The twin and the matrix lattices are oriented to have specific directions aligned with the global *x*-*y*-*z* axes ($\vec{e}_x, \vec{e}_y, \vec{e}_z$ unit vectors) of the simulation box. For the twin, we align the following directions: $\vec{e}_x||[011]$, $\vec{e}_y||[\bar{8}3\bar{3}]_{\mathrm{T}}$ and $\vec{e}_z||n_{(\bar{3}\bar{4}4),\mathrm{T}}$. For the matrix, we align the directions as $\vec{e}_x||[011]$, $\vec{e}_y||[8\bar{3}3]_{\mathrm{M}}$ and $\vec{e}_z||n_{(34\bar{4}),\mathrm{M}}$, ensuring the Type II twin symmetry. The subscripts T or M indicate that the crystallographic directions are referenced to the unit cell lattice vectors in the twin or the matrix respectively. The [011] direction (which is the twinning direction η_1 for the Type II TB) of the twin and the matrix are aligned. Let C_{LAT} represent a 3×3 matrix whose columns give the *x*-*y*-*z* components of the lattice vectors of the unit cell. Then for the twin and matrix phases, we have:

$$C^T_{LAT} = \begin{pmatrix} -0.1165 & 3.0248 & 3.3354 \\ -1.9885 & 2.0474 & -2.0474 \\ -1.8213 & -2.4284 & 2.4284 \end{pmatrix};$$

$$C^M_{LAT} = \begin{pmatrix} -0.1165 & 3.0248 & 3.3354 \\ 1.9885 & -2.0474 & 2.0474 \\ 1.8213 & 2.4284 & -2.4284 \end{pmatrix} \tag{2.1.1}$$

There are additional considerations in the creation of the simulation box, namely the absence of a crystallographic twin plane and the necessity of a lattice offset. The underlying analysis and methods of calculation are elaborated elsewhere [26]. A discussion of the same procedure here would require a significant digression and is instead briefly outlined in Appendix A. Given that the *x* and *y* directions are crystallographic, periodic boundary conditions are chosen for the lateral boundaries (across *xz* and *yz* planar boundaries of the simulation box). Note that the *z* direction is not a rational crystallographic direction as it is the normal to the $(34\bar{4})$ plane, i.e. $\vec{e}_z||n_{(34\bar{4}),\mathrm{M}}$, and not the direction $[34\bar{4}]$. Consequently, we do not apply periodic boundary conditions along z and shrink-wrapped conditions are employed across this boundary. On the top and the bottom, a layer of width 6Å (higher than the potential's cut-off value $r_c = 5.2$ Å) is frozen in position with the assumption that the atoms farther away from the twin boundary are representative of the bulk structure in the twin/matrix phases and are relatively unaffected by the relaxation. Having constructed the structure and specified these conditions, the conjugate gradient relaxation scheme in LAMMPS is employed specifying the tolerance for energy convergence as 1.0×10^{-8} (fractional change of energy between successive iterations should be lower than this value for convergence). Representative snapshots of the unrelaxed and relaxed structures are presented in Fig. 2(a). The atomistic potential energy of the T-W model is calculated as 4.19 J/m² and is quoted later in Table 1.

For the T-D model, the energy evaluation is two-step. First is the determination of the relaxed potential energy of the $(11\bar{1})$ terraces. Second is the augmentation of this value with the core energy of a twinning disconnection. The energy of the $(11\bar{1})$ terrace is determined identical to that of the $(34\bar{4})$ plane described above. The orientation of the twin variant is chosen such that $\vec{e}_x||[011]$, $\vec{e}_y||[\bar{2}1\bar{1}]_{\mathrm{T}}$ and $\vec{e}_z||n_{(\bar{1}\bar{1}1),\mathrm{T}}$. For the matrix, we align the directions as $\vec{e}_x||[011]$, $\vec{e}_y||[2\bar{1}1]_{\mathrm{M}}$ and $\vec{e}_z||n_{(11\bar{1}),\mathrm{M}}$, ensuring the Type II twin symmetry. Since the *x* and *y* directions are crystallographic, periodic boundary conditions are enforced along them (i.e. across the *xz* and *yz* planar boundaries of the simulation box). The *z* direction is not a rational crystallographic direction as it is normal to the $(11\bar{1})_{\mathrm{M}}$ plane, i.e. $\vec{e}_z||n_{(11\bar{1}),\mathrm{M}}$, and not the rational direction $[11\bar{1}]_{\mathrm{M}}$. We do not apply periodic boundary conditions along *z* and shrink-wrapped conditions are employed instead.

A key aspect in this crystallography is that with the [011] directions of both variants aligned, the vectors $[\bar{2}1\bar{1}]_T$ and $[2\bar{1}1]_M$ do

Table 1
Interface energy of the Type II TB.

Multi-scale Energetics of Topological Nanostructures	Continuum Strain Energy (J/m^2)	Atomistic Potential Energy (J/m^2)	Total Energy(J/m^2)
Terrace-Disconnection (T-D) Model	5.05×10^{-4}	2.69 (lower)	2.69 (preferred)
Tilt-Wall (T-W) Model	5.82×10^{-7} (lower)	4.19	4.19

not align. An in-plane shear γ_{xy}coherence strain must be applied to have the directions aligned such that $\vec{e}_y||[2\bar{1}1]_M||[\bar{2}1\bar{1}]_T$. This is described in detail in [26] and a further discussion is not necessary for the purposes of this study. The unit cell lattice vectors of the coherently strained lattices required for the chosen orientation on the {111} terrace is given by the matrices:

$$C^T_{LAT} = \begin{pmatrix} -0.1326 & 3.0475 & 3.3127 \\ -1.6954 & 2.3858 & -2.3858 \\ -2.0968 & -2.0968 & 2.0968 \end{pmatrix};$$

$$C^M_{LAT} = \begin{pmatrix} -0.1326 & 3.0475 & 3.3127 \\ 1.6954 & -2.3858 & 2.3858 \\ 2.0968 & 2.0968 & -2.0968 \end{pmatrix}. \quad (2.1.2)$$

Note that a similar consideration was not necessary in the T-W model because the shear-mismatch between $[\bar{8}3\bar{3}]_T$ and $[8\bar{3}3]_M$ is found to be negligibly small i.e. $\gamma_{xy} \approx 0$. The same boundary conditions and relaxation routines mentioned before are followed. Representative snapshots of the unrelaxed and relaxed structures are presented in Fig. 2(b). The atomistic potential energy of the $(11\bar{1})$ terrace in the T-D model is calculated as $2.424 J/m^2$. A detailed account of constructing the twinning disconnection for the T-D structure can be found in [13] and is briefly presented here. It is done by assembling two $(11\bar{1})$ terraces side by side (along $y||\langle 211\rangle$) with the terraces separated along z by one interplanar spacing ($d_{\{111\}} = 2.097$ Å). Then the anisotropic displacement field of an isolated twinning dislocation (calculated using the Eshelby-Stroh formalism as described in section 2.2 and Appendix A) are superimposed around the core. The structure is relaxed under governance of the interatomic potential to yield the equilibrium core structure of the twinning disconnection. This is represented in Fig. 2(c), only showing the positions of the Ti-atoms for clarity. The Ti-atoms are color-coded in a specific way (refer [13] for further details) to emphasize the disconnection. A supplementary video file (*VideoSuppl_TwinDisconMotion.mp4*) is also provided to show the simulated motion of the disconnection under external shear. The potential energy of the core is determined from selection of atoms within a cylinder around the center of the disconnection (axis aligned with the dislocation line) bounded by a radius slightly over $R = 5|b_{TD}|$. If sampling a larger radius it must be remembered that contributions from strain-energy of the dislocation will also contribute to the energy. Since the continuum evaluation (refer 2.2) is done independent of this atomistic evaluation, the choice of a large radius is not necessary. The core-energy of the twinning disconnection contributes $0.264\ J/m^2$ to the atomistic energy of the T-D nanostructure. In total, the atomistic potential energy of the T-D nanostructure comes out to be $2.69\ J/m^2$ as quoted in Table 1.

2.2. Evaluation of continuum strain energies for both Tilt-Wall (T-W) and Terrace-Disconnection (T-D) nanostructures

Both the T-D and T-W nanostructural models consist of an array of interface dislocations. The strain-field of isolated interface dislocations must first be determined. The matrix and twin phases are constituted by the highly anisotropic monoclinic B19′phase of NiTi. Hence, the Eshelby-Stroh formalism [44] is applied with the theory of anisotropic strain-fields of interface dislocation arrays [49]. The coordinate system is defined by a triad of vectors $\hat{t} - \hat{m} - \hat{n}$, where $\hat{t}||[011]_M = [011]_T, \hat{m}||[2\bar{1}1]_M = [\bar{2}1\bar{1}]_T, \hat{n}||n_{(11\bar{1}),M} = n_{(\bar{1}\bar{1}1),T}$ for the T-D model and $\hat{t}||[\bar{8}3\bar{3}]_M = [8\bar{3}3]_T, \hat{m}||[011]_M = [011]_T$, $\hat{n}||n_{(34\bar{4}),M} = n_{(\bar{3}\bar{4}4),T}$ for the T-W model. The choice of this triad is not arbitrary but follows a certain convention in the Eshelby-Stroh formalism [44]. By convention, we choose $\hat{m}$ to be on the slip plane pointing away from the direction of the dislocated half-space (of the interface twinning dislocation). Secondly, $\hat{n}$ is chosen to point from the matrix to the twin, i.e. the slip plane normal pointing toward the dislocated half-space (refer Fig. B1 in Appendix B). In this system, the displacement-field $u_i (i = 1, 2, 3)$ (and consequently the strain-field) is defined by a set of complex constants given by the expressions:

$$u^T_i(\mathbf{x}) = \frac{1}{2\pi\sqrt{-1}} \sum_{\alpha=1}^{6} A^T_{i\alpha} E^T_\alpha \ln\left(\hat{m}.\mathbf{x} + p^T_\alpha \hat{n}.\mathbf{x}\right) \quad \left(\hat{n}.\mathbf{x} > 0\right)$$

$$u^M_i(\mathbf{x}) = \frac{1}{2\pi\sqrt{-1}} \sum_{\alpha=1}^{6} A^M_{i\alpha} E^M_\alpha \ln\left(\hat{m}.\mathbf{x} + p^M_\alpha \hat{n}.\mathbf{x}\right) \quad \left(\hat{n}.\mathbf{x} < 0\right) \quad (2.2.1)$$

where $A_{i\alpha}$, E_α, p_α are the Eshelby-Stroh constants and the superscripts M and T stand for the matrix and twin phases respectively. The equations used to determine the Eshelby-Stroh constants and their corresponding values are detailed in Appendix B. Next, the strain-field of a dislocation array needs to be computed. We follow the approach in [49], given for homogeneous anisotropic materials and adapt it to the present case of an interface between distinct anisotropic phases. If dislocations with Burgers vector $\vec{b}$ are positioned periodically on the interface with a spacing d, then the spatially varying strain-field can be analytically computed and shown to reflect the same periodicity. The dislocation Burgers vectors and periodic spacings are: ($\vec{b}_{TD} = [0.7066, 0, 0]$ Å, $d_{TD} = 36.8$ Å) for the T-D model (following [26]) and ($\vec{b}_{TW} = [0, 0, 0.86]$ Å, $d_{TW} = 3.07$ Å) for the T-W model (following [25]). The ensuing calculations are done in the twin phase, keeping in mind that twin-symmetry (and also a assumption of equal volume fraction which is removed later) affords a symmetric partitioning of energy between the two phases, allowing the convenience of only calculating one of them. The spatially varying displacement gradient in the twin phase ($\hat{n}.\mathbf{x} > 0$) is given by:

$$u^T_{j,l}(\mathbf{x}) = \frac{1}{2d\sqrt{-1}} \sum_{\alpha=1}^{6} A^T_{j\alpha} E^T_\alpha \left(m_l + p^T_\alpha n_l\right) \cot\left(\frac{\pi}{d}\left(\hat{m}.\mathbf{x} + p^T_\alpha \hat{n}.\mathbf{x}\right)\right) \quad (2.2.2)$$

The far-field strains generated by an anisotropic dislocation array is non-zero and would render the strain-energy divergent. This is a non-trivial aspect and is discussed in [49]. We present, for the first time (to the best of the authors' knowledge), a framework to account for these far-field gradients in computing the interface strain energy. The non-zero far-field displacement gradient

$(\hat{n}.\mathbf{x} \to \pm\infty)$ is given by:

$$u_{j,l}^{T,far} = \frac{-1}{2d}\sum_{\alpha=1}^{6}\eta_\alpha A_{j\alpha}^T E_\alpha^T\left(m_l + p_\alpha^T n_l\right) \quad \left(\hat{n}.x \to \infty\right)$$
$$u_{j,l}^{M,far} = \frac{1}{2d}\sum_{\alpha=1}^{6}\eta_\alpha A_{j\alpha}^M E_\alpha^M\left(m_l + p_\alpha^M n_l\right) \quad \left(\hat{n}.x \to -\infty\right) \tag{2.2.3}$$

It can be shown that $\sum_{\alpha=1}^{6}\eta_\alpha A_{j\alpha}^T E_\alpha^T = -\sum_{\alpha=1}^{6}\eta_\alpha A_{j\alpha}^M E_\alpha^M \approx b_j$, due to twin-symmetry and the displacement-jump condition (4.6). This equality is approximate because there are additional terms due to the anisotropic constants. The approximation is reasonable because the additional terms are at least an order of magnitude lower for all TBs considered in this study. Consequently, the far-field gradient can be approximated to:

$$\begin{aligned} u_{j,l}^{T,far} &= \frac{-1}{2d}\left(b_j m_l + \sum_{\alpha=1}^{6}\eta_\alpha A_{j\alpha}^T E_\alpha^T p_\alpha^T n_l\right) \\ u_{j,l}^{M,far} &= \frac{1}{2d}\left(b_j m_l + \sum_{\alpha=1}^{6}\eta_\alpha A_{j\alpha}^M E_\alpha^M p_\alpha^M n_l\right) \end{aligned} \tag{2.2.4}$$

Note that the first of the terms is the component which falls out from the tensor $(\frac{\vec{b}}{2d}\otimes(-\hat{m}))$. Intuitively, this terms represents a shear displacement gradient introduced in the twin due to interface dislocations of magnitude $\vec{b}$, spaced periodically along $(-\hat{m})$ by spacing d. The direction is written as $(-\hat{m})$ because this direction points toward the dislocated half-space. Hence, for the dislocation array, it points towards the direction in which the displacement introduced by each interface dislocation is accumulating (refer Fig. B1(c) in Appendix B). This interpretation will be used later in Section 2.3. The contributions from the second term of (2.2.4) are found to be considerably lower (for all three TBs considered in the study). For the purposes of the theory developed in Section 2.3, we ignore this second term and approximate the far-field displacement-gradient (introduced by the interface dislocation array) as $(\frac{\vec{b}}{2d}\otimes(-\hat{m}))$.

The far-field displacement-gradients (given by (2.2.3) or (2.2.4)) can be eliminated in the following way. The initial strained state can be imposed on the system before insertion of the interface dislocation array. Both the twin and the matrix can be subject to a homogeneous deformation arising out of a linear displacement field given by:

$$u_j^T(\mathbf{x}) = \frac{1}{2d}\sum_{\alpha=1}^{6}\eta_\alpha A_{j\alpha}^T E_\alpha^T\left(\hat{m}.\mathbf{x} + p_\alpha^T\hat{n}.\mathbf{x}\right) \quad \left(\hat{n}.\mathbf{x} > 0\right)$$
$$u_j^M(\mathbf{x}) = \frac{-1}{2d}\sum_{\alpha=1}^{6}\eta_\alpha A_{j\alpha}^M E_\alpha^M\left(\hat{m}.\mathbf{x} + p_\alpha^M\hat{n}.\mathbf{x}\right) \quad \left(\hat{n}.\mathbf{x} < 0\right) \tag{2.2.5}$$

Note that these displacement fields can be appended with a rigid-body translation with no change to the strains or the strain-energies. Hence, they are unique up to a rigid translation. What is of more physical interest is the displacement gradient which is given by:

$$u_{j,l}^T = \frac{1}{2d}\sum_{\alpha=1}^{6}\eta_\alpha A_{j\alpha}^T E_\alpha^T\left(m_l + p_\alpha^T n_l\right) \quad \left(\hat{n}.\mathbf{x} > 0\right)$$
$$u_{j,l}^M = \frac{-1}{2d}\sum_{\alpha=1}^{6}\eta_\alpha A_{j\alpha}^M E_\alpha^M\left(m_l + p_\alpha^M n_l\right) \quad \left(\hat{n}.\mathbf{x} < 0\right) \tag{2.2.6}$$

The continuity of tractions are ensured by the fact that the chosen Eshelby-Stroh constants adhere to the conditions (4.5) and (4.7). The displacement gradients however are not continuous. On the interface, the discontinuity in the in-plane displacement gradients (i.e. only consider the in-plane terms of (2.2.6), which are nothing but terms with $n_l = 0$) is given by:

$$\begin{aligned} \left[u_{j,l}\right]^{in-plane} &= u_{j,l}^{T,in-plane} - u_{j,l}^{M,in-plane} \\ &= \frac{1}{2d}\sum_{\alpha=1}^{6}\left(\eta_\alpha A_{j\alpha}^T E_\alpha^T m_l + \eta_\alpha A_{j\alpha}^M E_\alpha^M m_l\right) = \left(\frac{b_j m_l}{d}\right) \end{aligned} \tag{2.2.7}$$

This follows from (4.6). A closer inspection would reveal that this is but a re-statement of the Frank-Bilby equation [43] (briefly outlined in Appendix C). The displacement gradients given by (2.2.6) are coherence displacement gradients required for atomic registry on the interface. We can also compute the total discontinuity in interface displacement-gradients (in-plane and out-of-plane) as:

$$\left[u_{j,l}\right] = u_{j,l}^T - u_{j,l}^M = \left(\frac{b_j m_l}{d}\right) + \frac{1}{2d}\left(\eta_\alpha A_{j\alpha}^T E_\alpha^T p_\alpha^T n_l + \eta_\alpha A_{j\alpha}^M E_\alpha^M p_\alpha^M n_l\right) \tag{2.2.8}$$

In the T-D model, the in-plane shear gradient $[u_{j,l}]_\gamma$ required for terrace coherence on $(11\bar{1})$ is

$$\left[u_{j,l}\right]_\gamma^{in-plane} = \begin{pmatrix} 0 & \gamma_{12} & 0 \\ 0 & 0 & 0 \\ 0 & 0 & 0 \end{pmatrix} \tag{2.2.9}$$

where $\gamma_{12} = 1.92\%$ [26]. In the case of the T-W model the in-plane coherence gradient $[u_{j,l}]_\alpha^{in-plane}$ is part of the total rotational misorientation $[u_{j,l}]_\alpha$ between the phases,

$$\begin{aligned} \left[u_{j,l}\right]_\alpha^{in-plane} &= \begin{pmatrix} 0 & 0 & 0 \\ 0 & 0 & 0 \\ 0 & -2\tan\alpha & 0 \end{pmatrix} \\ \left[u_{j,l}\right]_\alpha &= \begin{pmatrix} 0 & 0 & 0 \\ 0 & 0 & 2\tan\alpha \\ 0 & -2\tan\alpha & 0 \end{pmatrix} \end{aligned} \tag{2.2.10}$$

where $\alpha = 7.98^o$ [25] (also, $s = 2\tan\alpha = 0.280$ is the *classical* twinning shear). Hence, in both models, the two variants must be coherently strained for atomic registry (with these coherence strains also satisfying the traction continuity) following which the introduction of the interface dislocation array relieves the coherence strain away from the interface, rendering $u_{j,l}^{far} = 0$ in the matrix and twin phases. An illustration is provided to visualize this process in Appendix D. The net-inhomogeneous displacement-gradient $u_{j,l}(\mathbf{x})$ which is used to obtain the strain-field $(\varepsilon_{jl}(\mathbf{x}) = 0.5(u_{j,l} + u_{l,j}))$ and consequently strain-energy density $(e(\mathbf{x}) = {}^1\!/_2 C_{ijkl}\varepsilon_{ij}\varepsilon_{kl})$ is given by:

$$\begin{aligned} u_{j,l}^T(\mathbf{x}) = \frac{1}{2d\sqrt{-1}}\sum_{\alpha=1}^{6}A_{j\alpha}^T E_\alpha^T\left(m_l + p_\alpha^T n_l\right)\Bigg(\cot\left(\frac{\pi}{d}(\hat{m}.\mathbf{x} + p_\alpha^T\hat{n}.\mathbf{x})\right) \\ +\eta_\alpha\sqrt{-1}\Bigg) \end{aligned} \tag{2.2.11}$$

The distributions of continuum strain-energy densities are presented in Fig. 3 (a, b). The T-W nanostructure exhibits a highly localized strain-field in stark contrast to the T-D nanostructure whose strain-fields exhibit a larger domain of influence away from the TB. A converged strain-energy estimate can be obtained by integrating the densities to sufficiently large distances away from the interface. A distance of $z = 10$ nm was sufficient for both T-D and T-W nanostructures. Integrated strain-energies presented in Table 1 favor the T-W nanostructure whose strain-energy is orders of magnitude lower than the T-D strain energy. However, the atomic potential energy of both topologies (evaluated in Section 2.1) are orders of magnitude higher than their respective macro-scale strain-energy. It is the decisive criterion which ultimately favors a T-D topology over a T-W topology for the nanostructure of the Type II TB.

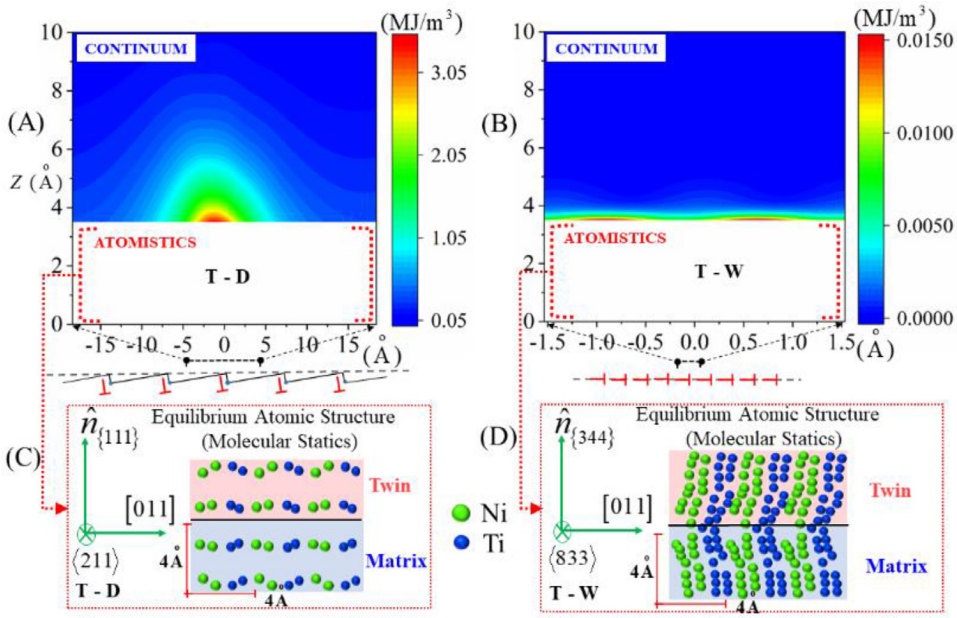

Fig. 3. Continuum and atomistic energies of TB nanostructures: (a) Strain-energy density distribution of the T-D model exhibiting larger domain of influence and higher strain energy as compared to the (b) T-W model (The fields are plotted beyond a cut-off distance, away from dislocation cores). (c) Equilibriated atomic structure on $(11\bar{1})$ terraces of the T-D structure exhibiting low distortion in atomic positions. (d) Equilibriated atomic structure on the $(34\bar{4})$ T-W exhibiting high distortions and consequently higher atomistic energy (Note that, in (c, d), not all atoms are on the plane of the figure). (For interpretation of the references to colour in this figure legend, the reader is referred to the web version of this article.)

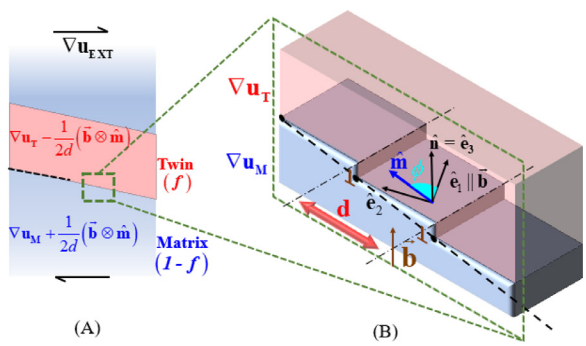

Fig. 4. Elements of the Evolving Interface theory: (a) Schematized microstructure representing a twin of volume fraction f growing in the matrix; ∇u_{EXT} represents the external microstructural deformation (strain) and the individual tensor expressions in the twin and matrix represent the bulk deformations sustained by each respectively (refer terms in Eq. (2.3.7)). (b) Schematized nanostructure of the TB, representing the $(\hat{e}_1 - \hat{e}_2 - \hat{e}_3)$ coordinate frame, the Burgers vector of the dislocations $\vec{b}$, the direction of the spacing $\hat{m}$, normal to the terrace planes $\hat{n}$, and coherence gradients $\nabla u_{T,M}$ sustained by the twin and matrix phases respectively on the terrace.

2.3. Evolving Interface theory: Dependence of TB topology on external strain and twin volume fraction

A theoretical framework is developed to determine the energy-minimal T-D nanostructure under external strain, enforced as an external displacement gradient ∇u_{EXT}. This is done for all major classes of deformation TBs i.e. Type II, Type I and Compound, continuing with NiTi as the study target. While the energy-optimality of the T-D topology for the Type II TB has been established, we treat both {111} Type I and {001} Compound TBs in NiTi as T-D topologies with dislocation spacings $d = \infty$. The crystallographic identity of the terrace plane (with normal $\hat{n}$), the step height of the disconnection, h, dislocation spacing, d, and the unit vector along this spacing, $\hat{m}$, together parametrize the nanostructure (Fig. 4). The Burgers vector of the dislocation is calculated using $\vec{b} = sh\hat{\eta}_1$ [4], where s is the twinning shear and $\hat{\eta}_1$ is the direction of shear, both well-defined "twinning elements" known for all TBs [21].

We first define a coordinate system using the triad of vectors $\hat{e}_1 = \vec{b}/|\vec{b}|$, $\hat{e}_3 = \hat{n}$ (TB normal pointing into the twin), and $\hat{e}_2 = \hat{n} \times \hat{t}$. There are two variables which define the T-D nanostructure: (1) the vector $\hat{m}$ on the terrace plane which is perpendicular to the dislocation line and which, if positioned at a disconnection, points from the twin phase into the matrix phase (i.e. points away the dislocated space, following the same convention as in section 2.2, also clarified in Fig. B1) (2) the spacing d along this vector. Since the vector $\hat{m}$ is a unit vector on the terrace plane, it can be replaced with a scalar ϕ parameter where

$$\hat{m} = \hat{e}_1 \cos\phi + \hat{e}_2 \sin\phi \tag{2.3.1}$$

and $-\pi \le \phi \le \pi$. Hence, we treat the T-D nanostructure as being parametrized by the pair of scalar variables (d, ϕ). Say, we begin with a specific value-pair fixing the T-D nanostructure. Under external ∇u_{EXT}, the deformation partitions (not necessarily in a symmetric manner) between the matrix and the twin phases. We presume that the twin and the matrix sustain the homogeneous gradients given by ∇u_T and ∇u_M respectively. Also, the components are given as $(\nabla u_{T,M})_{ij} = \frac{\partial u_i^{T,M}}{\partial x_j}$. These homogeneous gradients in conjunction with the far-field gradient introduced by the interface dislocation array together determine the net strain in the matrix and twin phases, and consequently the strain-energy. Given the T-D nanostructure i.e. (d, ϕ), we have 18 components of the two displacement gradients to solve for.

First, we need to establish the coherence deformation/strain. Coherence strain is the necessary deformation to ensure atomic registry on the terraces. This concept, proposed in the Topological Modeling framework [43] is generalized by us to a coherence displacement gradient (which will include both strains and in-plane rotations). We first partition the individual displacement gradients into an in-plane component and an out-of-plane component. For

instance, in the twin-phase, we can write:

$$\left(\nabla u_T^{in-plane}\right) = \begin{pmatrix} \frac{\partial u_1^T}{\partial x_1} & \frac{\partial u_1^T}{\partial x_2} & 0 \\ \frac{\partial u_2^T}{\partial x_1} & \frac{\partial u_2^T}{\partial x_2} & 0 \\ \frac{\partial u_3^T}{\partial x_1} & \frac{\partial u_3^T}{\partial x_2} & 0 \end{pmatrix} \tag{2.3.2}$$

$$\left(\nabla u_T^{out-plane}\right) = \begin{pmatrix} 0 & 0 & \frac{\partial u_1^T}{\partial x_3} \\ 0 & 0 & \frac{\partial u_2^T}{\partial x_3} \\ 0 & 0 & \frac{\partial u_3^T}{\partial x_3} \end{pmatrix} \tag{2.3.3}$$

$$\nabla u_T = \nabla u_T^{in-plane} + \nabla u_T^{out-plane} \tag{2.3.4}$$

The coherence condition can then be written as

$$\nabla u_T^{in-plane} - \nabla u_M^{in-plane} = \nabla u_{coh} \tag{2.3.5}$$

where ∇u_{coh} is the coherence gradient unique to the parent crystal structure and the twin boundary type. While $\nabla u_{coh} = O_{3\times3}$(zero) for Type I and Compound twin modes, for the Type II TB in NiTi we have:

$$\nabla u_{coh}^{Type-II} = \begin{pmatrix} 0 & \gamma_{12} & 0 \\ 0 & 0 & 0 \\ 0 & 0 & 0 \end{pmatrix} \tag{2.3.6}$$

where $\gamma_{12} = 4.90\%$. Next, we have the average strain-condition which is essentially enforcing a boundary condition on the microstructure, for its average deformation. This can be written as

$$(1-f)\left(\nabla u_M + \frac{1}{2d}\left(\vec{b}\otimes\hat{m}\right)\right) + f\left(\nabla u_T - \frac{1}{2d}\left(\vec{b}\otimes\hat{m}\right)\right) = \nabla u_{EXT} \tag{2.3.7}$$

where f is the volume fraction of the twin that can take values from 0 to 1. Note that, in (2.3.7), we augment the coherence displacement gradient with the far-field displacement gradient introduced by the dislocation array, in the matrix and twin phases. For instance, the far-field gradient in the twin is approximated as $-\frac{1}{2d}(\vec{b}\otimes\hat{m})$, motivated by the derivation in section 2.2 (Eq. (2.2.4)). Now, if partitioned to the in-plane and out-of-plane components, we have:

$$(1-f)\left(\nabla u_M^{in-plane} + \frac{1}{2d}\left(\vec{b}\otimes\hat{m}\right)\right) + f\left(\nabla u_T^{in-plane} - \frac{1}{2d}\left(\vec{b}\otimes\hat{m}\right)\right) = \nabla u_{EXT}^{in-plane} \tag{2.3.8}$$

and

$$(1-f)\left(\nabla u_M^{out-plane}\right) + f\left(\nabla u_T^{out-plane}\right) = \nabla u_{EXT}^{out-plane} \tag{2.3.9}$$

Now, (2.3.5) and (2.3.8) together result in:

$$\begin{aligned} \nabla u_T^{in-plane} &= \nabla u_{EXT}^{in-plane} + (1-f)\nabla u_{coh} + (2f-1)\tfrac{1}{2d}\left(\vec{b}\otimes\hat{m}\right) \\ \nabla u_M^{in-plane} &= \nabla u_T^{in-plane} - \nabla u_{coh} \end{aligned} \tag{2.3.10}$$

This determines 12 out of the initial 18 components in the displacement-gradients. Now consider the remaining 6 out-of-plane components of the external deformation (i.e. in $\nabla u_M^{out-plane}$and $\nabla u_T^{out-plane}$). We enforce traction continuity across the terrace and necessitate the condition:

$$(\mathbf{C_M}\varepsilon_M)\hat{n} = (\mathbf{C_T}\varepsilon_T)\hat{n} \tag{2.3.11}$$

where $\varepsilon_M = (\nabla u_M)_{\mathbf{SYM}}$ and $\varepsilon_T = (\nabla u_T)_{\mathbf{SYM}}$ are the strains on the terrace and $\mathbf{C_{M,T}}$represent the elasticity tensor of the matrix and twin respectively. Note that the terrace strains include no contribution from the strain-field of the interface dislocation array. The equations (2.3.9) and (2.3.11) determine the final 6 components, ultimately determining the complete ∇u_T and ∇u_M displacement gradients.

The theory has thus far established that, given the (d, ϕ) parameters of the nanostructure, a complete determination of the displacement gradients in the matrix and twin phases is possible, under any general external deformation ∇u_{EXT}. Hence, we can write them as functions of these parameters i.e. $\nabla u_T(d, \phi)$ and $\nabla u_M(d, \phi)$. It follows, that the net strain in the bulk of the matrix and twin phases are also functions of the same parameters i.e.:

$$\begin{aligned} e_T &= e_T(d,\phi) = \left(\nabla u_T(d,\phi) - \tfrac{1}{2d}\left(\vec{b}\otimes\hat{m}(\phi)\right)\right)_{\mathbf{SYM}} \\ e_M &= e_M(d,\phi) = \left(\nabla u_M(d,\phi) + \tfrac{1}{2d}\left(\vec{b}\otimes\hat{m}(\phi)\right)\right)_{\mathbf{SYM}} \end{aligned} \tag{2.3.12}$$

Now, we state the converse problem: Given an external imposed deformation ∇u_{EXT}, we want to determine the T-D nanostructure (i.e. the parameters d and ϕ) which minimizes the microstructural strain-energy:

$$E(d,\phi) = (1-f)\left(\frac{1}{2}e_M{:}\mathbf{C_M}e_M\right) + f\left(\frac{1}{2}e_T{:}\mathbf{C_T}e_T\right) \tag{2.3.13}$$

To illustrate the behavior, varying displacement gradients ∇u_{EXT} are applied to the TBs, with the strain magnitude parametrized by γ. For a range of strain values, the nanostructure (as parametrized by (d, ϕ)) minimizing the average microstructural energy is computed. Results are further interpreted as an angle of deviation from the terrace plane, calculated as $\theta = \tan^{-1}(h/d)$. This metric is presented as it ties with trace analysis methods in microscopy used to determine the Miller indices of the interface (for example, in Fig. 1(a, b)). Each value of θ corresponds to a different identity of the interface. The results are presented in Fig. 5.

3. Discussions

The current study first establishes the topology of the Type II TB with least interface energy. This is done by combining nanoscale continuum strain-energies with sub-nanoscale atomistic potential-energies. Continuum strain-energy considerations are typical of prominent classical defect theories which would invariably prefer the T-W topology. This agrees with historical understanding of the tilt-boundary as a low-energy grain boundary that only introduces a rotational misorientation between grains without strain. The advent of atomistic simulation tools, being more recent in this history, introduces new criteria for evaluation. The atomic potential energy dominates the strain-energy of the nanostructures and ultimately favors the T-D topology for the Type II TB's nanostructure, in stark contrast to classical expectations.

One of the challenges in atomistic modeling of Type II TBs is the irrationality of the interface which results in limited periodicity. For instance, for the [011] Type II TB of NiTi with $K_1 = (0.7205\ 1\ \bar{1})$, the interface is periodic along [011] and not along any other rational crystallographic direction. This presents a challenge for a computationally efficient implementation within an atomistic framework as periodic boundary conditions cannot be applied easily. In our approach, we have circumvented this challenge to model both TB nanostructures. For the T-W model, we have chosen a close rational approximant of the Type II plane $(0.7205\ 1\ \bar{1}) \approx (34\bar{4}) = (0.75\ 1\ \bar{1})$ that has been suggested before [37]. Periodic boundary conditions can now be imposed on this plane as elaborated in Section 2.1. Constructing the variants in the respective crystallographies described in the section effectively introduces a rotational misorientation on this plane, faithfully capturing the features of the nanostructure as proposed in [23,25]. For the T-D model, we stake that it is not necessary to simulate the exact irrational plane. The structure is constituted of $(11\bar{1})$ rational terrace planes with periodically spaced twinning disconnections.

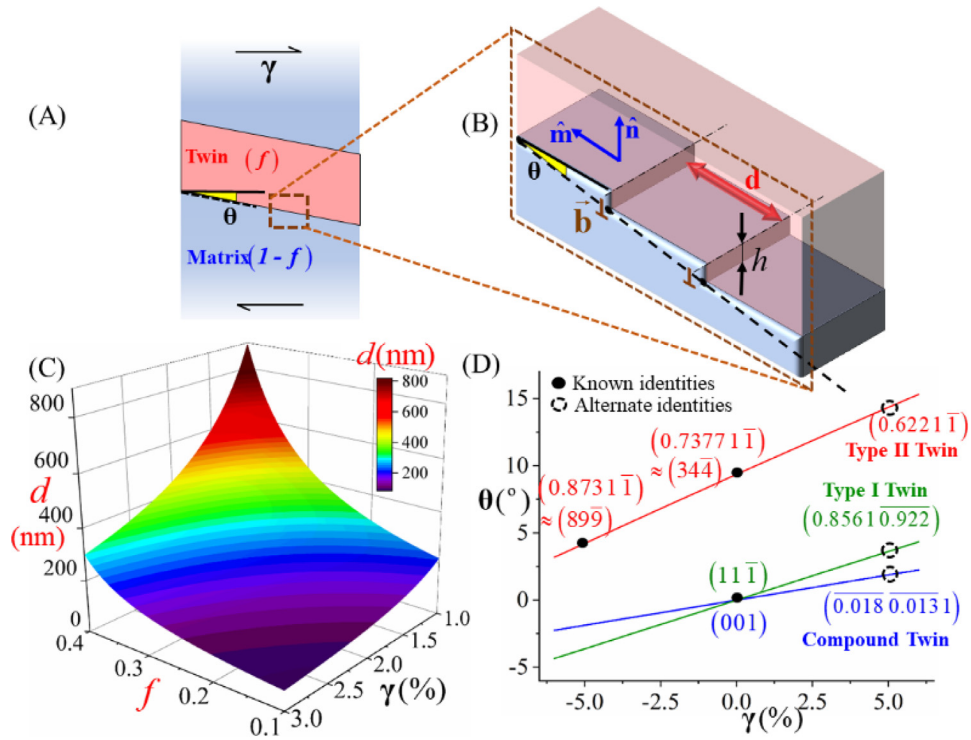

Fig. 5. Evolution of T-D nanostructure as a function of strain and twin volume fraction: (a) Schematized microstructure representing a twin of volume fraction f growing in the matrix, with the TB's trace making an angle θ with a reference crystallographic plane (chosen to be the terrace plane). (b) The T-D nanostructure of the TB constituting terrace planes (with normal $\hat{n}$) separated by disconnections (height h and Burgers vector $\bar{b}$) spaced at distance d along unit vector $\hat{m}$.(c) Sensitivity of the spacing d to external strain and microstructural volume fraction exhibiting over an 8-fold change in dislocation spacing and consequently the planar dislocation density on the TB (example chosen here is the (001) compound TB in NiTi under external deformation $\nabla u_{EXT} = \gamma(\hat{\eta}_1 \otimes \hat{\eta}_1)$). (d) Strain sensitivity of TBs permitting an evolution across a continuous spectrum of indicial identities (enforced displacement gradients are chosen as $\nabla u_{EXT}^{\text{TypeII}} = \gamma(\hat{n} \otimes \hat{n})$ and $\nabla u_{EXT}^{\text{Type-I,Compound}} = \gamma(\hat{\eta}_1 \otimes \hat{n})$, assuming $f = 0.5$), establishing the known contrasting identities of the Type II TB as experimental evidence of distinct states across this spectrum.

The irrationality is the result of periodically spaced twinning disconnections. The twinning disconnections are spaced at distances of tens of angstroms which are far higher than the Burgers vector magnitude of the twinning disconnection [26]. Consequently, the disconnections are sufficiently far that we can ignore any potential energy contribution due to core interaction between the disconnections. They only interact via their continuum strain-fields which is accounted for by the analytical methods described in section 2.2. Thus, by treating the rational terrace and the disconnection disjointly, and by accounting for the strain-energy of the periodic dislocation array, the calculation of energies for the T-D model of the Type II TB can be performed faithfully without having to construct the exact irrational plane in an atomistic framework.

Intuitively, the reason behind the high potential energy of the T-W model is the close spacing of dislocation cores (on consecutive (011) slip planes) arranging on a $(34\bar{4}) \approx (0.7205\ 1\ \bar{1})$ plane with very low atomic planar density. Consequently, the potential energy of the interface is considerably high, relaxing to the highly distorted atomic structure of Fig. 2(a). If a better rational approximation to the irrational plane was made for the nanostructure, for instance by choosing the rational approximants $(72\ 100\ \overline{100}) = (18\ 25\ \overline{25})$ or $(7205\ 10^4\ \overline{10^4}) = (1441\ 2000\ \overline{2000})$ etc., the resulting potential energies would be higher because the atomic planar densities of these approximants are lower. Thus, in the limit of the irrational plane, it is plausible that the atomistic potential energy will still be higher than what we have computed on the $(34\bar{4})$ plane. This would only further support the conclusion of this study that the T-W model has a higher interface potential energy without the need to simulate the exact irrational plane $(0.7205\ 1\ \bar{1})$. The choice of the TB to prefer a T-D topology is rooted in the preference of nearest {111}planes for their high planar density. It is the same reason behind preference of this family of planes in slip/twinning of FCC materials. However, there is a coherence strain necessitated on the {111} terrace which the interface relieves by accommodating a periodic array of dislocations. Hence, instead of a coherent TB residing on $(11\bar{1})$, the TB prefers to be semi-coherent and optimally balances the strain-energies and atomistic potential energies. Since, the twinning disconnections reside on a rational crystallographic plane, their nucleation and migration can be considered much in the same way as is proposed for the Type I TB [23,25].

While such a T-D topology was previously considered by the authors for the ⟨011⟩ Type II TB [26], an interface identity closer to $(89\bar{9})$ was found, matching only one set of experimental observations [38]. The key parameter which dictates the indicial identity is the periodic spacing between two consecutive dislocations. In the model of [26], the topology is described by $(d = 36.86\,\mathring{A}, \phi = \pi/2)$ explaining the indicial identity of $(89\bar{9})$ for the interface (dashed line in Fig. 1(c)). This prediction, done within the framework of the atomistic approach, employs material lattice constants reproducible by the underlying interatomic potential [47]. These constants deviate from experimental measures by 2.70%, on average. In Molecular Statics/Dynamics, this discrepancy would generally be considered minor as it is a formidable task for modern interatomic potentials to exactly reproduce measured lattice constants. This is particularly the case with phase-transforming materials such as NiTi, where the potential must account for physical parameters (cohesive energies, elastic moduli etc.) associated with multiple phases, inevitably leading to admittance of minor discrepancies in the lattice constants or unit cell motif positions (prevalent in other potentials developed for NiTi [47,50-56] as well). However, such deviations can critically influence the coherence strains and the dislocation spacing in the T-D model. We find that with the use of experimental lattice constants [57] in the model, the dislocation

spacing is significantly lower at ($d = 13.2\,\mathring{A}, \phi = \pi/2$). This yields an effective interface identified by the indices $(0.7377\ 1\ \bar{1}) \approx (34\bar{4})$. Hence, the T-D topological model agrees closely with the experimental observations of [37,39,40,42], albeit there is a slight deviation from prediction of the classical theory (i.e. $(0.7205\ 1\ \bar{1})$). It must be mentioned that this deviation is quite minor. Similar minor deviations between classical/phenomenological theory and modern topological theory has been shown and explained for other interfaces [58]. Given this change in topology, it is worth re-evaluating the strain-energy of the T-D nanostructure. With ($d = 13.2\,\mathring{A}, \phi = \pi/2$), the strain-energy can be recomputed using methods of section 2.2 as $1.1 \times 10^{-4}\,\mathrm{J/m^2}$ lower than the value quoted in Table 1. This magnitude is still orders lower than the atomistic potential energies and further supports the conclusion that the T-D nanostructure is energetically more favorable than the T-W nanostructure. However, while the proposed theory explains the $(34\bar{4})$ identity, the alternate observation of the Type II TB with indices $(89\bar{9})$ [38,41] is yet to be explained.

The T-D nanostructure can portray multiple different indicial identities contingent on the spacing between consecutive dislocations (refer Fig. 5(a, b)). Further, the nanostructure can seamlessly transition between these identities by glide of dislocations on the terraces. For instance, if dislocation-glide increases spacing from $d = 13.2\,\mathring{A}$ to $d = 34.21\,\mathring{A}$, identity changes to $(89\bar{9})$. We propose, for the first time, that the experimental observations (Fig. 1(a, b)) do not disagree but have fortuitously caught the interface in different equilibrium states gleaning an inherent ability of the interface to evolve across them. The interface is proposed to evolve in response to external strain which in the experimental studies previously referenced [37-42] could come from local residual strain in the sample. Note that such strains are only external to the interface topology but local to the microstructure. Such strains are inevitably introduced during the sample's mechanical/thermal loading history or TEM sample preparation. Microstructural heterogeneities such as the presence of multiple martensitic twin variants (for instance, this can be seen in the bright-field micrographs of analyzed samples in [37,41,42]), precipitates or grain boundaries can significantly elevate local strains (to the order of few percent) [59,60]. This is particularly plausible in shape memory alloys such as NiTi, where external macroscopic strains under pseudoelastic transformation easily exceed 5% [61-63]. At such strain levels or upon unload from such strains it can be expected that local elastic strains of the same order can be locked in the microstructure. In fact, local microstructural strains of such order have been measured around precipitates in NiTi [64,65] using the Geometric Phase Analysis (GPA) method [66,67]. In addition to such heterogeneities, there can also be a compounded effect due to unsymmetric twin volume fraction (i.e. twin volume fraction is not equal to the matrix volume fraction or $f \neq 0.5$), the exact value of which can significantly affect the dislocation-spacing and consequently the interface identity. Wide variation of f, from 2.09 to 5.57 has been previously reported for the [011] Type II Twin [68]. Consequently, an "Evolving Interface" (EI) theory is forwarded to establish these sensitivities to strain and volume fraction showing how it follows from energy minimization. A general framework is developed showing this capability in the three major classes of TBs [21]: Type I TBs, Type II TBs and Compound TBs, continuing with NiTi as the study target.

In order to develop a general framework applicable to all TBs, we idealize the twinning disconnection's Burgers vector as $\vec{b} = sh\hat{\eta}_1$ (with step height equal to one interplanar spacing, h). However, it is well-recognized that a disconnection can span multiple interplanar spacings and, in general, we have $\vec{b} = qsh\hat{\eta}_1$[4], where q is a positive integer. The exact step height is determined by the energy degeneracy between consecutive terraces separated by the disconnection [26] and is not a topological quantity [69]. However, for the present study, it turns out that if the Burgers vector scales up by a factor of $q > 1$, then the spacing between the disconnections commensurately increases i.e. $d \to qd$, conserving the $\vec{b}/d$ ratio. And with the step height scaling up as qh, the slope of the interface $\theta = \tan^{-1} h/d$ will also remain the same, keeping the same identity for the interface. Hence, the predictions of the theory are not affected by the multiplicity (q) of the elementary twinning dislocation ($\vec{b} = sh\hat{\eta}_1$). Only the exact dislocation spacing (and consequently the interface dislocation-density) would be affected (Fig. 4(c)). We include a calculation of the Burgers vector based on the Topological Modeling framework in Appendix E for the sake of completion. It can be verified that all calculated Burgers vector satisfy the condition $\vec{b} = qsh\hat{\eta}_1$.

The adoption of T-D topologies by Type I and Compound twins in their migration/growth is already recognized [23,24]. However, in equilibrium, their respective TB topologies are accepted as being completely coherent, residing on rational crystallographic planes with no disconnections. The proposed theory suggests that the equilibrium state can transition between coherent and semi-coherent topologies depending on the local strain-state around the interface. Consequently, they can adopt T-D topologies with finite dislocation-spacing $d < \infty$ and give the impression of an irrational-indexed interface. In fact, under small strains, the dislocation-spacing can change quite significantly and alter the dislocation-density ($\rho \sim 1/d$) on the interface (about 8-fold in Fig. 5(c)). Further, their observed traces on micrographs can be at angles that are significantly off from the expected crystallographic plane (refer Fig. 5(d)). The question remains as to why the topologies evolve under strain. The Topological Model predicts fixed interface topologies with the premise that the dislocation-array cannot have any long-range strain fields. This is based on strain-energy considerations that the interface's strain-energy will become divergent. Consequently, the predicted topologies are presumed not to interact with external strain and hence retain fixed topologies. However, we claim that it is energetically favorable for the interface to interact with external strain to further reduce energy. The energy to be minimized is not only the interface strain-energy but the average microstructural energy per unit volume. The latter energy includes the strain-energy of the interface dislocation array coupled with external strain applied on the microstructure.

We use the example of the Type II twin to show that it is energetically favorable for the interface nanostructure to cause non-zero long-range strain-fields in the presence of an external strain. We apply the external deformation $\nabla u_{EXT}^{\mathrm{TypeII}} = \gamma\,(\hat{n} \otimes \hat{n})$. When $\gamma = 0$, i.e. in the absence of external strain, it can be shown that

$$\nabla u_T^{in-plane} = -\nabla u_M^{in-plane} = \nabla u_{coh}/2 \tag{3.1}$$

In other words, the coherence strain is equally partitioned between the twin and the matrix. This is one of the assumptions in our previous work [26]. The strain-fields from the interface dislocations exactly nullify this coherence gradient in the matrix and twin phases yielding no long-range strains i.e.

$$\begin{aligned} e_T &= \left(\nabla u_{\mathrm{T}}^{in-plane} - \tfrac{1}{2d}\left(\vec{b} \otimes \hat{m}\right)\right)_{\mathbf{SYM}} = 0 \\ e_M &= \left(\nabla u_{\mathrm{M}}^{in-plane} + \tfrac{1}{2d}\left(\vec{b} \otimes \hat{m}\right)\right)_{\mathbf{SYM}} = 0 \end{aligned} \tag{3.2}$$

For this condition, we get the energy-minimal nanostructure with ($d = 13.25\,\mathring{A}, \phi = \pi/2$). This nanostructure does not generate any long-range fields and hence does not interact with external microstructural strain. However, we find that in the presence of external strain on the nanostructure, the coherence strain is not necessarily equally partitioned. Such an unequal partitioning has been recognized across phase interfaces involving significant elastic mismatch [70]. However, it is unexpected for cases where we have twin symmetry, where both phases are of the same crystal structure and nearly equal elastic constitution (there is a slight

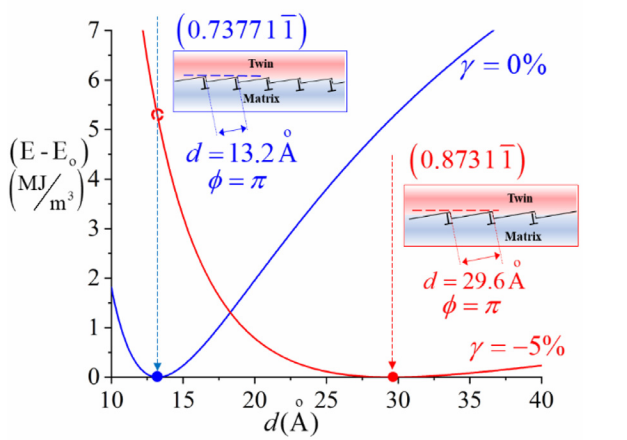

Fig. 6. Variation of microstructural strain-energy (the minima of each plot is taken to be the reference value E_o, to facilitate comparison of both plots with the same scale) against dislocation spacing; The blue dotted arrow indicates the spacing, and the consequent nanostructure, which is energy-minimal at no applied strain ($\gamma = 0\%$) and produces no net long-range strain-fields; In the presence of external strain however, it is energetically favorable for the configuration to reduce energy further by evolving to the state indicated by the red-dotted arrow, allowing the nanostructure to have long-range strain fields. (For interpretation of the references to colour in this figure legend, the reader is referred to the web version of this article.)

difference in the elastic constants due to the different orientation of the twin with respect to the matrix). The proposed theory accounts for such unequal partitioning in the presence of external strain and varying volume fractions, an effect which has not been considered till date, to the best of the authors' knowledge. In the presence of external strain, the nanostructure evolves to a different state ($d = 29.6\,\mathring{A}, \phi = \pi/2$) where the long-range fields do not satisfy (3.2). This implies that long-range fields are generated by the nanostructure despite which the configuration obtained is energy-minimal. This effect is illustrated in Fig. 6.

Contrary to existing theories, we establish that it is energetically favorable for interface nanostructures to generate long-range strain fields. These fields couple with external microstructural strain to reduce energy (Fig. 6), ultimately responsible for the evolution of the T-D nanostructure to a different identity. This evolving capability is, to the best of the authors' knowledge, the only plausible explanation for the observations of the Type II TB in NiTi. Experimental evidences which were thus far considered contrasting (Fig. 1(a, b)) fit consistently as distinct states in a continuous spectrum of identities (Fig. 5(d)), fortuitously transposing as experimental evidence of the proposed evolving behavior. And given that this theory is built on fundamental equations in material mechanics and is devoid of any empiricism, it ensues that other TBs considered in the study also exhibit the same evolving capability. This theory is proposed as an extension to the Topological Modeling approach, allowing prediction of equilibrium T-D topologies under the influence of strain and varying volume fractions.

It is interesting to note that the Type II TB exhibits the highest sensitivity, followed by Type I TBs and then Compound TBs. This sensitivity is likely correlated to the high-known mobility of Type II TBs as compared to Type I TBs [24,71]. The change of TB dislocation-density in dependence of elastic external strain is significant in the field of Shape Memory Alloys (SMAs), as it is likely a key factor in the mechanism of slip emission [13,72,73]. Note that this behavior of the twin interface is disjoint from twin growth or twin propagation accommodating external strain. Whether or not the twin grows under external strain, the current study proposes that if the strain is held at a non-zero value, either externally or residually locked in the local microstructure (even after external unloading), the broad faces of the twin would not remain constant but reorient due to a change in the interface disconnection density. If we have an externally applied stress, there can be local relaxation due to twin growth/shrinkage (twin boundary motion). This would change the prevailing elastic strain on the twin boundary as the twin grows/shrinks, but the magnitude remains finitely non-zero under the applied stress. Hence, the boundary orientation also evolves according to the local strain evolution. Nevertheless, the T-D model parameters respond to this strain state based on the same approach. We further propose that this behavior will be exhibited by any crystalline interface that migrates via diffusionless dislocation-mediated mechanisms (e.g. habit planes), consequently adopting T-D topological nanostructures in the presence of external strain. We establish that the interfaces can evolve to varying identities, exhibiting traces on micrographs at varying slopes (i.e. Fig. 5(a, d)). A recent example of such change was observed in Ni-Mn-Ga, where the trace of internal twin boundaries in the martensite phase showed significant deviation from its expected crystallographic plane [74]. This observation was made in the vicinity of the habit plane where the lattice-mismatch between the austenite-martensite phases gave rise to significant strains (calculated to be of the order of few percent). These strains may also be augmented due to the well-known elastic softening prior to the martensitic transformation [75-78], further influencing the local twin interface topology as proposed in this study. Furthermore, this study elevates the role of such interfaces in experimental characterization, allowing a measure of local interface slope to quantify local microstructural strain (strain-mapping).

4. Conclusions

This study proposes to reconcile the debated nanostructure of the Type II TB in NiTi using energy-considerations on both atomistic and continuum scales. Among the T-W and T-D topologies that have thus far been proposed, it is shown that the T-D topology is energy-minimal primarily because the atomic potential energy of this topology is lower. Subsequently, an "Evolving Interface" theory is developed to establish the strain-sensitivity of the T-D topology. The framework is developed for all major deformation twin modes in general (Type I, Type II and Compound) and applied to examples of each twinning mode in NiTi. It is shown that under the coupled influence of microstructural strain and local twin volume fraction, the T-D topology can evolve to a different identity. This is achieved by dislocation-glide on the terrace planes, consequently changing the dislocation-density on the TB and the slope of its trace (say, on a micrograph). It is proposed that such an evolution has been indirectly evidenced by observation of contrasting identities of the Type II TB in NiTi. The theory is proposed as an extension to the Topological Modeling framework allowing the determination of equilibrium topologies under the influence of strain. The implications of such an evolving behavior in experimental characterization of interfaces and in functional materials have been discussed.

Declaration of Competing Interest

The authors declare that they have no known competing financial interests or personal relationships that could have appeared to influence the work reported in this paper.

Acknowledgements

The work is supported by Air Force Office of Scientific Research (AFOSR) under award number FA9550–18–1–0198, with Dr. Ali Sayir as Program Director, which is gratefully acknowledged. The use of the Illinois Campus Cluster, a computing resource that is operated by the Illinois Campus Cluster Program (ICCP) in conjunction with the National Center for Supercomputing Applications

(NCSA) and which is supported by funds from the University of Illinois at Urbana-Champaign, is also gratefully acknowledged.

Supplementary materials

Supplementary material associated with this article can be found, in the online version, at doi:10.1016/j.actamat.2021.116716.

Appendix A: Construction of Twin Boundary atomic structure for atomistic simulation

This appendix briefly outlines the construction of atomic structures for the atomistic simulations described in Section 2.1. The unit cell lattice constants and motif positions are chosen consistent with the interatomic potential [47]. Fig. A1 represents the unit cell, where a Ti atom is chosen on the lattice site and the remaining motif atoms are positioned accordingly. The lattice constants are $a = 2.699\,\mathring{A}$; $b = 4.386\,\mathring{A}$; $c = 4.606\,\mathring{A}$; $\beta = 93.41^o$, with the motif positions given in fractional coordinates (along the unit cell crystallographic directions): Ti$(0, 0, 0)$, Ti$(0.3413, 0.5, 0.6973)$, Ni$(0.6768, 0.5, 0.2067)$ and Ni$(0.6645, 0, 0.4906)$.

Now we detail the construction of the T-W structure. We start with the simulation box in Fig. A2(a) with global axes *x-y-z* (unit vectors $(\vec{e}_x, \vec{e}_y, \vec{e}_z)$ unit vectors) of the simulation box. The dimensions of the simulation box are specified in LAMMPS by a start and end coordinate. We define them as $(0, x_{\max})$, $(0, y_{\max})$, $(-{}^{z_{\max}}/_2, {}^{z_{\max}}/_2)$. The normal to the twin boundary is chosen to be parallel to the z-axis, i.e. $\vec{e}_z || n_{\{34\bar{4}\}}$. The choice of the z-axis limits is made with the notion of having the twin boundary at position $z = 0$. Hence, the twin variant is constructed in the region defined by the limits: $(0, x_{\max})$, $(0, y_{\max})$, $(0, {}^{z_{\max}}/_2)$. And the matrix is constructed in the region defined by the limits: $(0, x_{\max})$, $(0, y_{\max})$, $(-{}^{z_{\max}}/_2, 0)$. For the twin, we align the following directions: $\vec{e}_x || [011]$, $\vec{e}_y || [\bar{8}3\bar{3}]$ and $\vec{e}_z || n_{(\bar{3}\bar{4}4)}$. For the matrix, we align the directions as $\vec{e}_x || [011]$, $\vec{e}_y || [8\bar{3}3]$ and $\vec{e}_z || n_{(34\bar{4})}$. The dimensions of the simulation box are chosen to be $x_{\max} = 8L_{\langle 011\rangle} = 50.88\,\mathring{A}$, $y_{\max} = 2L_{\langle 833\rangle} = 56.38\,\mathring{A}$ and $z_{\max} = 2L_{\langle 344\rangle} = 49.62\,\mathring{A}$, where $L_{\langle uvw\rangle}$ represents the periodic lattice distance along any crystallographic direction in the family $\langle uvw\rangle$. The number of atoms in the simulation is $N \approx 10,500$, sufficiently large for the purposes of the study.

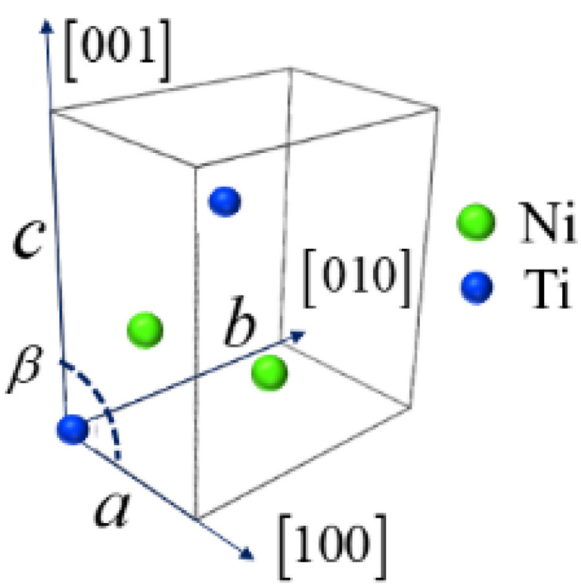

Fig. A1. Unit cell of B19′ NiTi martensite; The lattice constants and motif positions are chosen consistent with the interatomic potential [47] used for atomistic simulations.

The orientation of the lattice vectors required to achieve this crystallographic alignment is given by the $C_{LAT}^{T,M}$ matrices in Eq. (2.1.1). A more detailed description to calculate these matrices can be found in the appendices of [26]. The final parameter to be defined to complete construction of the twin is the *origin* of the twin and matrix regions in the simulation box. The origin simply specifies the position of a lattice site in the simulation box. It is used to specify the position of the lattice in the global coordinate system attached to the simulation box. The origin is specified in normalized coordinates $(\bar{x} = {}^{x}/_{|011|}, \bar{y} = {}^{y}/_{|833|}, \bar{z} = {}^{z}/_{|344|})$, where the normalization is done using the periodic lattice distance along the chosen axes. Hence, given the translational symmetry of the lattice over periodic lattice distances, origin values only in the range $(0 \le \bar{x} < 1, 0 \le \bar{y} < 1, 0 \le \bar{z} < 1)$ define unique positions of the lattice. Given that we want to create a twin and a matrix (i.e. two crystal lattices), we need to specify two origins. If the origins of both lattices are coincident, then there is no *lattice offset* between the two lattices. If the difference of origins is non-zero, then there exists a non-zero lattice offset between the two lattices. The concept of a lattice offset has long been known [4,20,79,80] and its necessity for the Type II TB has been discussed in detail in [26]. It is only briefly described here, as much is necessary to construct the atomic structure of twin-boundaries in this study. The origin of the matrix variant is chosen such that no atoms lie on the partitioning twin boundary at $z = 0$. This is shown in Fig. A2(b). This choice is consciously made because the twin-boundary is not a crystallographic plane accommodating atoms from both variants. The fundamental reason behind this is the incommensurate atomic structures of the two twin variants which cannot be reconciled to form a common atomic plane at the twin boundary. Once again, this has been discussed in detail in [26] and a further discussion is out of scope for the study and avoided here. The origin of the matrix is chosen as $O_M(0, 0, z_\varepsilon = 0.3)$. This choice of z_ε is not unique and another value can be chosen accordingly as long as it is ensured that the twin boundary is not a crystallographic plane with atoms. If the origin of the twin is chosen such that $O_T = O_M$, then there is no lattice offset. However, it is shown in [26] that there is a necessity for a non-zero lattice offset from crystallographic and energetic considerations. Following the procedure detailed in that study, the energy-minimizing lattice-offset for the twin variant can be calculated as $O_T - O_M = (0.688, 0.038, 0.006)$. The constructed twin-variant is shown in Fig. A2(c), and the relative position of both origins are shown in Fig. A2(d) to highlight the lattice offset. This is the atomic structure used in the simulation of the T-W model in Section 2.1.

For the atomic structure of the {111} terrace of the T-D topological model, the procedure followed is exactly that as specified in [26]. The twin is oriented such that $\vec{e}_x || [011]$, $\vec{e}_y || [\bar{2}1\bar{1}]$ and $\vec{e}_z || n_{(\bar{1}\bar{1}1)}$. For the matrix, we align the directions as $\vec{e}_x || [011]$, $\vec{e}_y || [2\bar{1}1]$ and $\vec{e}_z || n_{(11\bar{1})}$, ensuring the Type II twin symmetry. The lattice orientations are specified using the $C_{LAT}^{T,M}$ matrices in Eq. (2.1.2). The dimensions of the simulation box are chosen as $x_{\max} = 4L_{\langle 011\rangle} = 25.44\,\mathring{A}$, $y_{\max} = 10L_{\langle 211\rangle} = 81.63\,\mathring{A}$ and $z_{\max} = 20L_{\langle 111\rangle} = 125.81\,\mathring{A}$. The number of atoms in the simulation is $N = 19,200$, sufficiently large for the purposes of the study. The matrix origin is chosen as $O_M(0, 0, z_\varepsilon = 0.266)$, with the lattice offset given by $O_T - O_M = (0.522, 0.128, 0.048)$.

Appendix B. Calculation of Eshelby-Stroh constants to determine continuum strain-fields

In this section, we briefly outline the equations used to solve for the Eshelby-Stroh constants that are involved in determination of the strain-field and strain-energies of both nanostructures (in

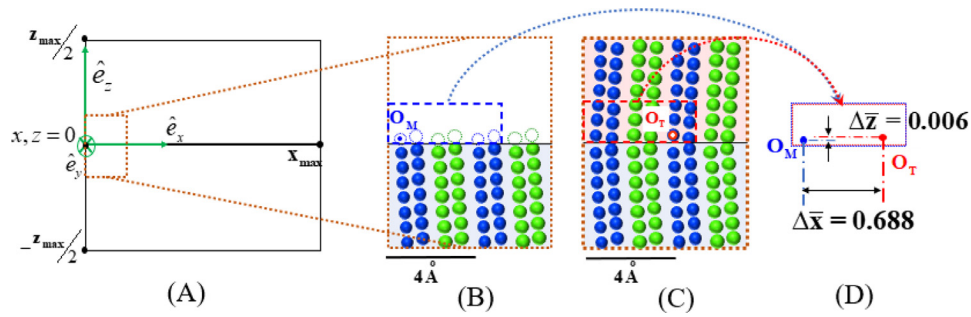

Fig. A2. Construction of T-W atomic-structure involving lattice offsets: (a) The simulation box is schematically represented with a boundary partitioning the matrix and twin variants. (b) The matrix is constructed by specifying origin O_M (only positive values of the origin are allowed, as defined in LAMMPS; the origin only specifies the relative position of the lattice inside the simulation box and the matrix atomic structure is only created below the twin boundary as intended). (c) The twin is constructed by specifying origin O_T. (d) Overlapped regions of the matrix and twin highlighting the lattice offset $O_T - O_M$; only the x-z offsets can be shown in this 2D projection and it must be noted that there is a y-offset involved as well.

Section 2.1). The constants $(p_\alpha, A_{i\alpha}), (\alpha = 1, 2, ..., 6)$ are obtained by solving equilibrium equations in both the phases. In the matrix phase for instance, we must have:

$$\sigma^M_{ij,j} = C^M_{ijkl} u^M_{k,lj} = 0 \tag{4.1}$$

This reduces to a set of algebraic equations given by,

$$C^M_{ijkl}(\mathrm{m}_i + p^M_\alpha \mathrm{n}_i)(\mathrm{m}_l + p^M_\alpha \mathrm{n}_l) A^M_{k\alpha} = 0 \tag{4.2}$$

And to have a non-trivial solution for$(p^M_\alpha, A^M_{i\alpha})$, it follows that:

$$\det\{C^M_{ijkl}(\mathrm{m}_i + p^M_\alpha \mathrm{n}_i)(\mathrm{m}_l + p^M_\alpha \mathrm{n}_l)\} = 0 \tag{4.3}$$

For eachp^M_α, we obtain a vector $A^M_{k\alpha}(k = 1, 2, 3)$ from equation (4.2). These complex constants appear as three conjugate pairs (i.e. three conjugate pairs in p_α and three conjugate vector pairs in $A_{k\alpha}$). It will be assumed henceforth that the constants are ordered such that the complex constants with positive imaginary parts have indices $\alpha = 1, 2, 3$, with their respective conjugates having indices $\alpha = 4, 5, 6$. The E_α constants for each phase are solved for by enforcing traction and displacement continuity across the slip plane. On the half-plane where $(\hat{n}.\mathbf{x}) = 0$ and $(\hat{m}.\mathbf{x}) > 0$, continuity of displacements and tractions are enforced through the following equations respectively:

$$\sum_{\alpha=1}^{6} A^T_{i\alpha} E^T_\alpha - \sum_{\alpha=1}^{6} A^M_{i\alpha} E^M_\alpha = 0 (\mathrm{i} = 1, 2, 3) \tag{4.4}$$

$$\sum_{\alpha=1}^{6} L^T_{i\alpha} E^T_\alpha - \sum_{\alpha=1}^{6} L^M_{i\alpha} E^M_\alpha = 0 (\mathrm{i} = 1, 2, 3) \tag{4.5}$$

For the half-plane where $(\hat{n}.\mathbf{x}) = 0$ and $(\hat{m}.\mathbf{x}) < 0$, a displacement jump associated with the Burgers vector is to be enforced as a discontinuity, while maintaining equality of tractions. This is respectively enforced by:

$$\sum_{\alpha=1}^{6} \eta_\alpha A^T_{i\alpha} E^T_\alpha + \sum_{\alpha=1}^{6} \eta_\alpha A^M_{i\alpha} E^M_\alpha = 2b_i \quad (\mathrm{i} = 1, 2, 3) \tag{4.6}$$

$$\sum_{\alpha=1}^{6} \eta_\alpha L^T_{i\alpha} E^T_\alpha + \sum_{\alpha=1}^{6} \eta_\alpha L^M_{i\alpha} E^M_\alpha = 0 \quad (\mathrm{i} = 1, 2, 3) \tag{4.7}$$

where, $\eta_\alpha = 1$ for $\alpha = 1, 2, 3$ and $\eta_\alpha = -1$ for $\alpha = 4, 5, 6$, and $L_{i\alpha}$ is given by

$$L^M_{i\alpha} = -n_j C^M_{ijkl}(\mathrm{m}_l + p^M_\alpha \mathrm{n}_l) A^M_{k\alpha} \tag{4.8}$$

The elastic constants are picked consistent to those reproducible by the interatomic potential [47]. For the T-D model, the Burgers vector is $\vec{b}_{TD} = [0.7066, 0, 0]\,\overset{0}{\mathrm{A}}$ [26] whereas for the T-W model it is $\vec{b}_{TW} \approx [0, 0, 0.86]\,\overset{0}{\mathrm{A}}$[25] in the respective chosen coordinate frame. The Eshelby-Stroh constants for the T-D and T-W dislocations are given in Tables A and B respectively (here $i=\sqrt{-1}$). The twin symmetry offers some simple relations between the constants.

Table A
Eshelby-Stroh Constants for T-D interface dislocation.

$p^T_1 = p^M_1$	−0.3273+1.3438i	$E^T_1 = -E^M_1$	−0.2204+0.0154i
$p^T_2 = p^M_2$	−0.3091+0.9710i	$E^T_2 = E^M_2$	0.3171−0.0462i
$p^T_3 = p^M_3$	0.2313+0.7117i	$E^T_3 = -E^M_3$	0.0848+0.0174i
$p^T_4 = p^M_4$	−0.3273−1.3438i	$E^T_4 = -E^M_4$	0.2204+0.0154i
$p^T_5 = p^M_5$	−0.3091−0.9710i	$E^T_5 = E^M_5$	−0.3171−0.0462i
$p^T_6 = p^M_6$	0.2312−0.7117i	$E^T_6 = -E^M_6$	−0.0848+0.0174i

Table B
Eshelby-Stroh Constants for T-W interface dislocation.

$p^T_1 = -p^M_4$	0.4988+1.1532i	$E^T_1 = E^M_4$	−0.2453+0.3714i
$p^T_2 = -p^M_5$	−0.5180+0.8425i	$E^T_2 = E^M_5$	0.4509+0.1573i
$p^T_3 = -p^M_6$	0.1543+0.8272i	$E^T_3 = -E^M_6$	−0.6041+0.1865i
$p^T_4 = -p^M_1$	0.4988−1.1532i	$E^T_4 = E^M_1$	0.2453+0.3714i
$p^T_5 = -p^M_2$	−0.5180−0.8425i	$E^T_5 = E^M_2$	−0.4509+0.1573i
$p^T_6 = -p^M_3$	0.1543−0.8272i	$E^T_6 = -E^M_3$	0.6041+0.1865i

The displacement-field of $\vec{b}_{TD}$ is plotted in Figure B1(b). The displacement component $u_1(\mathbf{x})$ is plotted as it is the major component of the screw-dislocation $\vec{b}_{TD} = [0.7066, 0, 0]\,\overset{0}{\mathrm{A}}$, in the T-D model. The triad of vectors $\hat{t} - \hat{m} - \hat{n}$ used in the formalism (here and in section 2.2) is indicated in the plot. In Figure B1(c), the expression for the far-field displacement-gradient from the dislocation array can be derived as $(\frac{\vec{b}}{2d} \otimes (-\hat{m}))$ (in the twin region).

This derivation is based on the simple notion that displacements are increasing by $\vec{b}$ for every d spacing, as we traverse along the vector $(-\hat{m})$. The term indicated is the major contributor to the far-field displacement gradient from the dislocation-array. There is a second-term involving the anisotropic Eshelby-Stroh constants (Eq. (2.2.4)), is known to be atleast an order lower in comparison to $(\frac{\vec{b}}{2d} \otimes (-\hat{m}))$ (refer section 2.2).

Appendix C. The Frank-Bilby equation

The Frank-Bilby equation gives the required defect/dislocation density on an interface required to relieve coherence strains on the interface. Suppose, $F_T = I + \nabla u_T$ is the coherence deformation gradient applied to the twin and $F_M = I + \nabla u_M$ is the coherence deformation gradient applied to the matrix. We take the example of the Type II TB terrace and the respective coherence gradients for atomic registry on the $(11\bar{1})_\mathrm{M} = (\bar{1}\bar{1}1)_\mathrm{T}$ terrace planes. Note that the displacement gradients $\nabla u_{\mathrm{T,M}}$ are the same as those referred to in Eq. (3.2). Also, $(\nabla u_\mathrm{T})_{jl} = u^\mathrm{T}_{j,l}$ and $(\nabla u_\mathrm{M})_{jl} = u^\mathrm{M}_{j,l}$ as used in Eq. (2.2.7). The Frank-Bilby equation [43] dictates that the dislocation-spacing d along a direction $\hat{m}$ (we pick the same def-

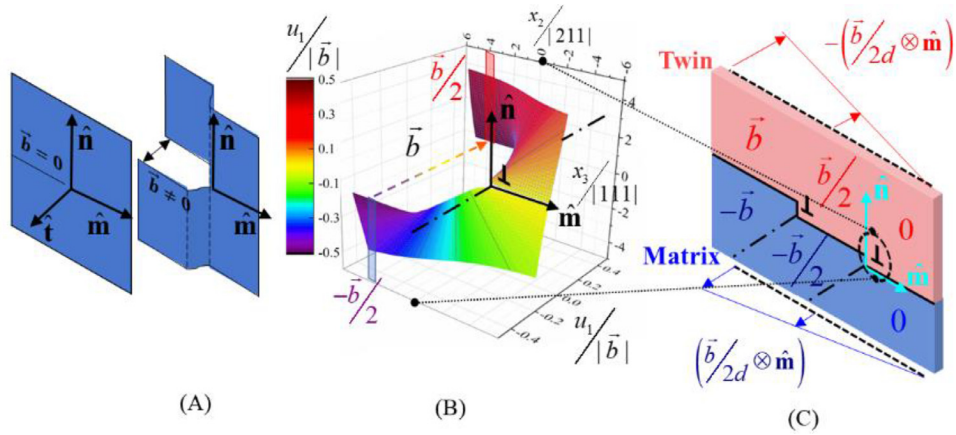

Fig. B1. Plot of anisotropic displacement-field of T-D twinning dislocation and far-field displacement-gradient caused by a periodic dislocation array: (a) Schematized screw-dislocation indicating the displacement discontinuity caused by a non-zero Burgers vector; the coordinate system triad $\hat{t} - \hat{m} - \hat{n}$ involved in the Eshelby-Stroh formalism (used in this appendix, section 2.2 and 2.3) is indicated; note that $\hat{m}$ points away from the dislocated half-space (figure adapted from [13]). (b) A plot of the $u_1(\mathbf{x})$ displacement component of the $\vec{b}_{TD}$ dislocation calculated from the Eshelby-Stroh formalism outlined in this appendix; the displacement disregistry sustained by the twin variant is $\vec{b}/2$ (with small spatial variations) and that sustained by the matrix is $-\vec{b}/2$ (figure adapted from [13]). (c) A notional derivation of the far-field displacement-gradient introduced by a periodic array of interface disconnections with Burgers vector $\vec{b}$, spaced at a distance d along $\hat{m}$; Arbitrarily choosing a reference region with zero displacements, the displacement-continuity introduced by each dislocation over its adjacent periodic spacing is augmented; this effectively translates to a far-field shear displacement gradient derived as $-(\frac{\vec{b}}{2d} \otimes \hat{m})$ in the twin and $(\frac{\vec{b}}{2d} \otimes \hat{m})$ in the matrix.

inition as adopted in section 2.2 and 2.3) required to nullify this coherence strain is given by:

$$-\left(F_{\mathrm{T}}^{-1} - F_{\mathrm{M}}^{-1}\right)\hat{m} = \frac{\vec{b}}{d} \tag{5.1}$$

With the linear-elastic approximation $F_{\mathrm{T,M}}^{-1} \approx I - \nabla u_{\mathrm{T,M}}$, this reduces to:

$$(\nabla u_{\mathrm{T}} - \nabla u_{\mathrm{M}}).\hat{m} = \frac{\vec{b}}{d} \tag{5.2}$$

This is equivalent to (2.2.7).

Appendix D. Illustration of in-plane coherence strains relieved by a periodic array of interface dislocations

We refer to Figure D1 to illustrate the necessity of in-plane coherence strains and how they are relieved by a periodic array of interface dislocations.

Appendix E. Calculation of the Burgers vector based on the Topological Modeling framework

In this section, the calculation of the Burgers vector through the Topological Modeling framework is shown for all TBs in this

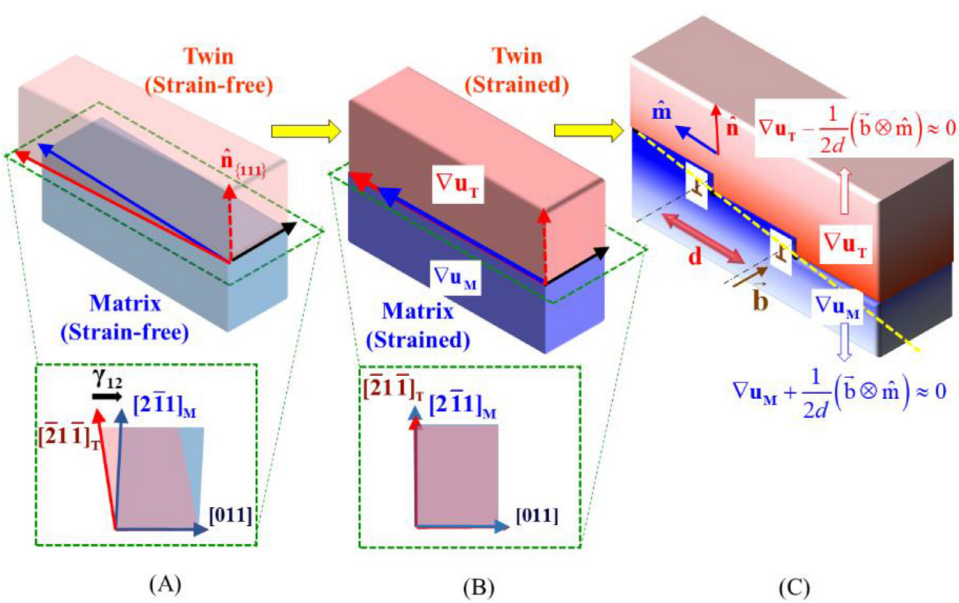

Fig. D1. Schematic illustration of the theoretical analysis in section 2.2, using the T-D model as the example (We presume zero external strain and equal volume fraction of the twin and the matrix): (a) The crystallography of the [011]Type II twin showing the matrix and twin variants in their strain-free configurations; With the common twinning direction $\eta_1 = [011]$ aligned, there is a shear-mismatch on the $(11\bar{1})_{\mathrm{M}}$ plane. (b) Coherence strains applied to matrix and twin variants for atomic registry on the terrace plane; the applied in-plane gradient for terrace coherence is $\nabla u_{\mathrm{T}} = -\nabla u_{\mathrm{M}} = {}^{1}/_{2}\nabla u_{coh}$ (refer Eq. (3.1)). (c) The coherence strains on the terrace are relieved by introduction of a periodic array of interface dislocations spaced by d; the far-field displacement gradient introduced by the dislocation array can be well-approximated by $\pm{}^{1}/_{2d}(\vec{b} \otimes \hat{m})$ as discussed in section 2.2 and in Appendix B.

study, for the sake of completion. The mathematical approach proposed in [69], adopted in several works including [23,25,35] has been employed. We begin by specifying the orientation of the matrix and twin variants with respect to a global coordinate frame $x-y-z$ ($\vec{e}_x, \vec{e}_y, \vec{e}_z$ unit vectors) of the simulation box similar to the setup in 2.1. The orientation of the matrix variant is specified by a 3×3 matrix C^M_{LAT}, where the columns of the matrix gives the coordinates of the 3 lattice vectors (of the martensitic unit cell in the global axes, similar to Section 2.1). This matrix is determined by aligning specific crystallographic directions along the global axes (discussed in Section 2.1, also elaborated further in an appendix in [26]). The chosen aligned directions for each TB type are listed in Table 1. Note that experimental lattice constants [57] (and not the lattice constants associated with the interatomic potential [47]) of B19′ NiTi are employed as in Section 2.3. Once C^M_{LAT} is obtained based on the chosen orientation, the orientation of the twin variant is determined by calculating the same matrix C^T_{LAT} for the twin. This is done by using equations from the classical theory of deformation twinning [21]. For the $\langle 011 \rangle$ type II TB, the symmetry relation is a 180° rotation about $\eta_1 = [011]$. Note that this direction is common between the matrix and twin variants and hence does not need further specification via a T or M subscript. The lattices are related to each other by the equation:

$$C^T_{LAT} = \left(2\left(\hat{\eta}_1 \otimes \hat{\eta}_1\right) - I\right) C^M_{LAT} \tag{6.1}$$

where $\hat{\eta}_1$ is the unit vector (specified in the global frame) along the twinning direction for the type II TB, which in this case is [011]. For the {111} type I twin, the symmetry relation is a reflection in $K_1 = (11\bar{1})_M$. The lattices are related to each other by the equation:

$$C^T_{LAT} = \left(I - 2\left(\hat{n} \otimes \hat{n}\right)\right) C^M_{LAT} \tag{6.2}$$

where $\hat{n}$ is the unit vector normal to K_1. For the compound twin, we can employ any one of the two symmetry relations above. We choose the type II symmetry relation about its twinning shear direction $\eta_1 = [100]_{\mathrm{M}}$. Table E1 lists the orientations lattices $C^{M,T}_{LAT}$ corresponding to the matrix and twin of all TB types. The Burgers vector is calculated by the equation:

$$\vec{b} = \left(\vec{t}_T - \vec{t}_M\right) \tag{6.3}$$

where it is presumed that all vectors are specified in the same global coordinate frame. For example, if the vector $\vec{t}_M = [uvw]_{\mathrm{M}}$ is specified in the crystallographic basis of the matrix, then to convert the vector to its global frame, we perform the matrix operation $\vec{t}_M = C^M_{LAT}\begin{pmatrix} u \\ v \\ w \end{pmatrix}$ to get the coordinates in the global frame (likewise for a vector specified in the twin frame). The vectors $\vec{t}_T$ and $\vec{t}_M$ are translational symmetry vectors in the twin and the matrix respectively. The step height is calculated by the equation:

$$h_D = \hat{n}.\vec{t}_M \tag{6.4}$$

where $\hat{n}$ is a normal vector pointing from the matrix to the twin. It is the normal to the twin plane in the case of the {111} type I twin and {001} compound twin and normal to the terrace planes in the case of the $\langle 011 \rangle$ type II twin. All results of the calculation are summarized in Table E1 below.

TB type	Global axes	C_{LAT}	$\vec{b} = (\vec{t}_T - \vec{t}_M)$	$h_D = \hat{n}.\vec{t}_M$ (Å)	$\vec{b}$ (Å)
.[011] Type- II	$\hat{e}_x \| [011]$ $\hat{e}_y \| [2\bar{1}1]_{\mathrm{M}}$ $\hat{e}_z \| \hat{n}_{(11\bar{1}),\mathrm{M}}$	$C^M_{LAT} = \begin{bmatrix} -0.3013 & 2.7946 & 3.3972 \\ 1.8755 & -2.1668 & 2.1668 \\ 2.1826 & 2.1826 & -2.1826 \end{bmatrix}$ $C^T_{LAT} = \begin{bmatrix} -0.3013 & 2.7946 & 3.3972 \\ -1.8755 & 2.1668 & -2.1668 \\ -2.1826 & -2.1826 & 2.1826 \end{bmatrix}$ (Involves terrace coherence strains)	$[001]_{\mathrm{T}} - [010]_{\mathrm{M}}$	$2.1826 = h_{(11\bar{1})}$	$\begin{pmatrix} 0.6026 \\ 0 \\ 0 \end{pmatrix} = s_{II} h_{(11\bar{1})} \hat{\eta}_1$ $\lVert\vec{b}\rVert = 0.6026$ Å
$(11\bar{1})$Type-I	$\hat{e}_x \| [011]_{\mathrm{M}}$ $\hat{e}_y \| [2\bar{1}1]_{\mathrm{M}}$ $\hat{e}_z \| \hat{n}_{(11\bar{1}),\mathrm{M}}$	$C^M_{LAT} = \begin{bmatrix} -0.2553 & 2.7415 & 3.4502 \\ 1.8755 & -2.1668 & 2.1668 \\ 2.1826 & 2.1826 & -2.1826 \end{bmatrix}$ $C^T_{LAT} = \begin{bmatrix} -0.2553 & 2.7415 & 3.4502 \\ 1.8755 & -2.1668 & 2.1668 \\ -2.1826 & -2.1826 & 2.1826 \end{bmatrix}$ (No coherence strains involved)	$[\bar{1}01]_{\mathrm{T}} - [110]_{\mathrm{M}}$	$4.3652 = 2h_{(11\bar{1})}$	$\begin{pmatrix} 1.2193 \\ 0.5826 \\ 0 \end{pmatrix} = 2 s_I h_{(11\bar{1})} \hat{\eta}_1$ $\lVert\vec{b}\rVert = 1.3513$ Å
(001)Compound	$\hat{e}_x \| [100]$ $\hat{e}_y \| [010]_{\mathrm{M}}$ $\hat{e}_z \| \hat{n}_{(001),\mathrm{M}}$	$C^M_{LAT} = \begin{bmatrix} 2.889 & 0 & -0.5473 \\ 0 & 4.12 & 0 \\ 0 & 0 & 4.5895 \end{bmatrix}$ $C^T_{LAT} = \begin{bmatrix} 2.889 & 0 & -0.5473 \\ 0 & -4.12 & 0 \\ 0 & 0 & -4.5895 \end{bmatrix}$ (No coherence strains involved)	$[00\bar{1}]_{\mathrm{T}} - [001]_{\mathrm{M}}$	$4.5895 = h_{(001)}$	$\begin{pmatrix} 1.0946 \\ 0 \\ 0 \end{pmatrix} = s_C h_{(001)} \hat{\eta}_1$ $\lVert\vec{b}\rVert = 1.0946$ Å

In Table E1, the direction $\hat{\eta}_1$ is a unit vector along the twinning direction for the TB (one of the classical twinning elements of the boundaries which can be obtained found in [46]). Note that the Burgers vector satisfy the equation based on the twinning shear justifying this choice in the approach of Section 2.3. It is also worth mentioning that the Type II TB has the least step height of the three TB types (Table E1). The step height has been proposed as a guide to quantify mobility of twinning disconnections [23], where a lower step height promotes higher TB mobility. Consequently, the calculation above indicates a higher mobility of Type II twins as compared to Type I and Compound twins. A complete calculation of the twin migration energetics, as done in [26,81,82] would establish this behavior more conclusively but is out of scope for the present study and is suggested for future work.

References

[1] I.J. Beyerlein, X. Zhang, A. Misra, Growth Twins and Deformation Twins in Metals, Annu. Rev. Mater. Res. 44 (1) (2014) 329–363.
[2] J. Wang, N. Li, O. Anderoglu, X. Zhang, A. Misra, J.Y. Huang, J.P. Hirth, Detwinning mechanisms for growth twins in face-centered cubic metals, Acta Mater. 58 (6) (2010) 2262–2270.
[3] S. Mahajan, D.F. Williams, Deformation twinning in metals and alloys, Int. Metallurg. Rev. 18 (2) (1973) 43–61.
[4] J.W. Christian, S. Mahajan, Deformation twinning, Prog. Mater Sci. 39 (1) (1995) 1–157.
[5] G. Arlt, Twinning in ferroelectric and ferroelastic ceramics: stress relief, J. Mater. Sci. 25 (6) (1990) 2655–2666.
[6] D.J. Barber, H.R. Wenk, Deformation twinning in calcite, dolomite, and other rhombohedral carbonates, Phys. Chem. Miner. 5 (2) (1979) 141–165.
[7] B. Li, K.M. Knowles, Molecular dynamics simulation of albite twinning and pericline twinning in low albite, Model. Simul. Mater. Sci. Eng. 21 (5) (2013) 055012.
[8] D. Xie, G. Hirth, J.P. Hirth, J. Wang, Defects in deformation twins in plagioclase, Phys. Chem. Miner. 46 (10) (2019) 959–975.
[9] K. Lu, Stabilizing nanostructures in metals using grain and twin boundary architectures, Nat. Rev. Mater. 1 (5) (2016) 16019.
[10] B. Gludovatz, A. Hohenwarter, D. Catoor, E.H. Chang, E.P. George, R.O. Ritchie, A fracture-resistant high-entropy alloy for cryogenic applications, Science 345 (6201) (2014) 1153.
[11] P. Chowdhury, H. Sehitoglu, R. Rateick, Recent advances in modeling fatigue cracks at microscale in the presence of high density coherent twin interfaces, Curr. Opin. Solid State Mater. Sci. 20 (3) (2016) 140–150.
[12] Y. Song, X. Chen, V. Dabade, T.W. Shield, R.D. James, Enhanced reversibility and unusual microstructure of a phase-transforming material, Nature 502 (7469) (2013) 85–88.
[13] A.S.K. Mohammed, H. Sehitoglu, Martensitic twin boundary migration as a source of irreversible slip in shape memory alloys, Acta Mater. 186 (2020) 50–67.
[14] R. Sidharth, W. Abuzaid, M. Vollmer, T. Niendorf, H. Sehitoglu, Fatigue Crack Initiation in the Iron-Based Shape Memory Alloy FeMnAlNiTi, Shape Memory and Superelasticity, 2020.
[15] T. Duerig, A. Pelton, D. Stöckel, An overview of nitinol medical applications, Mater. Sci. Eng.: A 273-275 (1999) 149–160.
[16] M. Gueltig, H. Ossmer, M. Ohtsuka, H. Miki, K. Tsuchiya, T. Takagi, M. Kohl, High frequency thermal energy harvesting using magnetic shape memory films, Adv. Energy Mater. 4 (17) (2014) 1400751.
[17] P. II, S. Benzing, J. Asnani, M. Vivake, Superelastic tire, U.S.P.T.O (Ed.) United States of America as Represented by the Administrator of National Aeronautics and Space Administration, United States, 2016.
[18] J.W. Christian, CHAPTER 20 - Deformation Twinning, in: J.W. Christian (Ed.), The Theory of Transformations in Metals and Alloys, Pergamon, Oxford, 2002, pp. 859–960.
[19] H.A. Khater, A. Serra, R.C. Pond, Atomic shearing and shuffling accompanying the motion of twinning disconnections in Zirconium, Philos. Mag. 93 (10–12) (2013) 1279–1298.
[20] J.P. Hirth, J. Wang, C.N. Tomé, Disconnections and other defects associated with twin interfaces, Prog. Mater Sci. 83 (2016) 417–471.
[21] B.A. Bilby, A.G. Crocker, The theory of the crystallography of deformation twinning, Proc. R. Soc. Lond. Series A. Math. Phys. Sci. 288 (1413) (1965) 240–255.
[22] A. Kelly, K.M. Knowles, in: Chapter 11 - Twinning, Crystallography and Crystal Defects, John Wiley & Sons Ltd., Chichester, UK, 2012, pp. 335–361.
[23] R.C. Pond, J.P. Hirth, Topological model of type II deformation twinning, Acta Mater. 151 (2018) 229–242.
[24] P. Müllner, Twinning stress of type I and type II deformation twins, Acta Mater. 176 (2019) 211–219.
[25] R.C. Pond, J.P. Hirth, K.M. Knowles, Topological model of type II deformation twinning in NiTi martensite, Philos. Mag. 99 (13) (2019) 1619–1632.
[26] A.S.K. Mohammed, H. Sehitoglu, Modeling the interface structure of type II twin boundary in B19′ NiTi from an atomistic and topological standpoint, Acta Mater. 183 (2020) 93–109.
[27] C. Maletta, E. Sgambitterra, F. Furgiuele, R. Casati, A. Tuissi, Fatigue of pseudoelastic NiTi within the stress-induced transformation regime: a modified Coffin–Manson approach, Smart Mater. Struct. 21 (11) (2012) 112001.
[28] A.R. Pelton, G.H. Huang, P. Moine, R. Sinclair, Effects of thermal cycling on microstructure and properties in Nitinol, Mater. Sci. Eng.: A 532 (2012) 130–138.
[29] Y. Gao, L. Casalena, M.L. Bowers, R.D. Noebe, M.J. Mills, Y. Wang, An origin of functional fatigue of shape memory alloys, Acta Mater. 126 (2017) 389–400.
[30] Y.F. Zheng, L.C. Zhao, H.Q. Ye, HREM studies of twin boundary structure in deformed martensite in the cold-rolled TiNi shape memory alloy, Mater. Sci. Eng.: A 297 (1) (2001) 185–196.
[31] P. Müllner, A.H. King, Deformation of hierarchically twinned martensite, Acta Mater. 58 (16) (2010) 5242–5261.
[32] N. Zárubová, Y. Ge, O. Heczko, S.P. Hannula, In situ TEM study of deformation twinning in Ni–Mn–Ga non-modulated martensite, Acta Mater. 61 (14) (2013) 5290–5299.
[33] O. Heczko, Understanding motion of twin boundary—a key to magnetic shape memory effect, IEEE Trans. Magn. 50 (11) (2014) 1–7.
[34] N. Zou, Z. Li, Y. Zhang, B. Yang, X. Zhao, C. Esling, L. Zuo, Plastic deformation of Ni–Mn–Ga 7M modulated martensite by twinning & detwinning and intermartensitic transformation, Int. J. Plast. 100 (2018) 1–13.
[35] B. Karki, P. Müllner, R. Pond, Topological model of type II deformation twinning in 10M Ni-Mn-Ga, Acta Mater. (2020).
[36] K. Adachi, J. Perkins, C.M. Wayman, Type II twins in self-accommodating martensite plate variants in a Cu-Zn-Al shape memory alloy, Acta Metall. 34 (12) (1986) 2471–2485.
[37] K.M. Knowles, D.A. Smith, The crystallography of the martensitic transformation in equiatomic nickel-titanium, Acta Metall. 29 (1) (1981) 101–110.
[38] Z.L. Xie, Y. Liu, HRTEM study of ⟨011⟩ type II twin in NiTi shape memory alloy, Philos. Mag. 84 (32) (2004) 3497–3507.
[39] K.M. Knowles, A high-resolution electron microscope study of nickel-titanium martensite, Philos. Mag. A 45 (3) (1982) 357–370.
[40] M. Nishida, K. Yamauchi, I. Itai, H. Ohgi, A. Chiba, High resolution electron microscopy studies of twin boundary structures in B19′ martensite in the Ti-Ni shape memory alloy, Acta Metall. Mater. 43 (3) (1995) 1229–1234.
[41] Y. Liu, Z.L. Xie, Twinning and detwinning of ⟨0 1 1⟩ type II twin in shape memory alloy, Acta Mater. 51 (18) (2003) 5529–5543.
[42] M. Nishida, T. Hara, M. Matsuda, S. Ii, Crystallography and morphology of various interfaces in Ti–Ni, Ti–Pd and Ni–Mn–Ga shape memory alloys, Mater. Sci. Eng.: A 481-482 (2008) 18–27.
[43] R.C. Pond, X. Ma, Y.W. Chai, J.P. HirthF.R.N. Nabarro, J.P. Hirth (Eds.), Chapter 74 topological modelling of martensitic transformations, Disloc. Solids, Elsevier (2007) 225–261.
[44] D.M. Barnett, J. Lothe, An image force theorem for dislocations in anisotropic bicrystals, J. Phys. F Met. Phys. 4 (10) (1974) 1618–1635.
[45] S. Plimpton, Fast parallel algorithms for short-range molecular dynamics, J. Comput. Phys. 117 (1) (1995) 1–19.
[46] K. Otsuka, X. Ren, Physical metallurgy of Ti–Ni-based shape memory alloys, Prog. Mater Sci. 50 (5) (2005) 511–678.
[47] G. Ren, H. Sehitoglu, Interatomic potential for the NiTi alloy and its application, Comput. Mater. Sci. 123 (2016) 19–25.
[48] A.P. Sutton, V. Vitek, J.W. Christian, On the structure of tilt grain boundaries in cubic metals I. symmetrical tilt boundaries, Philos. Trans. R. Soc. Lond. Series A, Math. Phys. Sci. 309 (1506) (1983) 1–36.
[49] J.P. Hirth, D.M. Barnett, J. Lothe, Stress fields of dislocation arrays at interfaces in bicrystals, Philos. Mag. A 40 (1) (1979) 39–47.
[50] W.S. Lai, B.X. Liu, Lattice stability of some Ni-Ti alloy phases versus their chemical composition and disordering, J. Phys. Condens. Matter 12 (5) (2000) L53–L60.
[51] H. Ishida, Y. Hiwatari, MD simulation of martensitic transformations in TiNi alloys with MEAM, Mol. Simul. 33 (4–5) (2007) 459–461.
[52] K. Saitoh, K. Kubota, T. Sato, Atomic-level structural change in Ni-Ti alloys under martensite and amorphous transformations, Technische Mechanik 30 (1–3) (2010) 269–279.
[53] Y. Zhong, K. Gall, T. Zhu, Atomistic study of nanotwins in NiTi shape memory alloys, J. Appl. Phys. 110 (3) (2011) 033532.
[54] Y. Zhong, K. Gall, T. Zhu, Atomistic characterization of pseudoelasticity and shape memory in NiTi nanopillars, Acta Mater. 60 (18) (2012) 6301–6311.
[55] W.-.S. Ko, B. Grabowski, J. Neugebauer, Development and application of a Ni-Ti interatomic potential with high predictive accuracy of the martensitic phase transition, Phys. Rev. B 92 (13) (2015) 134107.
[56] M. Muralles, S.-.D. Park, S.Y. Kim, B. Lee, Phase transformations, detwinning and superelasticity of shape-memory NiTi from MEAM with practical capability, Comput. Mater. Sci. 130 (2017) 138–143.
[57] K. Otsuka, T. Sawamura, K. Shimizu, Crystal structure and internal defects of equiatomic TiNi martensite, Physica Status Solidi(a) 5 (2) (1971) 457–470.
[58] R.C. Pond, S. Celotto, J.P. Hirth, A comparison of the phenomenological theory of martensitic transformations with a model based on interfacial defects, Acta Mater. 51 (18) (2003) 5385–5398.
[59] V.B. Ozdol, C. Gammer, X.G. Jin, P. Ercius, C. Ophus, J. Ciston, A.M. Minor, Strain mapping at nanometer resolution using advanced nano-beam electron diffraction, Appl. Phys. Lett. 106 (25) (2015) 253107.
[60] W.Z. Abuzaid, H. Sehitoglu, J. Lambros, Localisation of plastic strain at the microstructurlal level in Hastelloy X subjected to monotonic, fatigue, and creep loading: the role of grain boundaries and slip transmission, Mater. High Temp. 33 (4–5) (2016) 384–400.

[61] R. Delville, B. Malard, J. Pilch, P. Sittner, D. Schryvers, Transmission electron microscopy investigation of dislocation slip during superelastic cycling of Ni–Ti wires, Int. J. Plast. 27 (2) (2011) 282–297.
[62] A.P. Stebner, H.M. Paranjape, B. Clausen, L.C. Brinson, A.R. Pelton, In situ neutron diffraction studies of large monotonic deformations of superelastic nitinol, Shape Memory Superelast. 1 (2) (2015) 252–267.
[63] A.N. Bucsek, D. Dale, J.Y.P. Ko, Y. Chumlyakov, A.P. Stebner, Measuring stress-induced martensite microstructures using far-field high-energy diffraction microscopy, Acta Crystallogr., Sect. A 74 (5) (2018) 425–446.
[64] W. Tirry, D. Schryvers, Quantitative determination of strain fields around Ni4Ti3 precipitates in NiTi, Acta Mater. 53 (4) (2005) 1041–1049.
[65] W. Tirry, D. Schryvers, Linking a completely three-dimensional nanostrain to a structural transformation eigenstrain, Nat. Mater. 8 (9) (2009) 752–757.
[66] M.J. Hÿtch, J.-.L. Putaux, J.-.M. Pénisson, Measurement of the displacement field of dislocations to 0.03 Å by electron microscopy, Nature 423 (6937) (2003) 270–273.
[67] F. Brenne, A.S.K. Mohammed, H. Sehitoglu, High resolution atomic scale characterization of dislocations in high entropy alloys: critical assessment of template matching and geometric phase analysis, Ultramicroscopy 219 (2020) 113134.
[68] T. Onda, Y. Bando, T. Ohba, K. Otsuka, Electron Microscopy Study of Twins in Martensite in a Ti-50.0 at%Ni Alloy, Mater. Trans. 33 (4) (1992) 354–359 JIM.
[69] J.P. Hirth, R.C. Pond, Steps, dislocations and disconnections as interface defects relating to structure and phase transformations, Acta Mater. 44 (12) (1996) 4749–4763.
[70] A.J. Vattré, M.J. Demkowicz, Partitioning of elastic distortions at a semicoherent heterophase interface between anisotropic crystals, Acta Mater. 82 (2015) 234–243.
[71] L. Straka, A. Soroka, H. Seiner, H. Hänninen, A. Sozinov, Temperature dependence of twinning stress of Type I and Type II twins in 10M modulated Ni–Mn–Ga martensite, Scr. Mater. 67 (1) (2012) 25–28.
[72] S. Kajiwara, W.S. Owen, Substructure of austenite formed by a partial reverse martensitic transformation in an Fe-Pt alloy, Metall. Trans. 4 (8) (1973) 1988–1990.
[73] S. Kajiwara, T. Kikuchi, Dislocation structures produced by reverse martensitic transformation in a Cu-Zn alloy, Acta Metall. 30 (2) (1982) 589–598.
[74] E. Bronstein, E. Faran, D. Shilo, Analysis of austenite-martensite phase boundary and twinned microstructure in shape memory alloys: the role of twinning disconnections, Acta Mater. 164 (2019) 520–529.
[75] X. Ren, K. Otsuka, The role of softening in elastic constant c44 in martensitic transformation, Scr. Mater. 38 (11) (1998) 1669–1675.
[76] X. Ren, N. Miura, J. Zhang, K. Otsuka, K. Tanaka, M. Koiwa, T. Suzuki, Y.I. Chumlyakov, M. Asai, A comparative study of elastic constants of Ti–Ni-based alloys prior to martensitic transformation, Mater. Sci. Eng.: A 312 (1) (2001) 196–206.
[77] X. Ding, T. Suzuki, X. Ren, J. Sun, K. Otsuka, Precursors to stress-induced martensitic transformations and associated superelasticity: molecular dynamics simulations and an analytical theory, Phys. Rev. B 74 (10) (2006) 104111.
[78] X. Ding, J. Zhang, Y. Wang, Y. Zhou, T. Suzuki, J. Sun, K. Otsuka, X. Ren, Experimental study of elastic constant softening prior to stress-induced martensitic transformation, Phys. Rev. B 77 (17) (2008) 174103.
[79] P.D. Bristowe, A.G. Crocker, A computer simulation study of the structures of twin boundaries in body-centred cubic crystals, Philos. Mag.: J. Theoret. Exp. Appl. Phys. 31 (3) (1975) 503–517.
[80] R. Schweinfest, F. Ernst, T. Wagner, M. Rühle, High-precision assessment of interface lattice offset by quantitative HRTEM, J. Microsc. 194 (1) (1999) 142–151.
[81] T. Ezaz, H. Sehitoglu, Type II detwinning in NiTi, Appl. Phys. Lett. 98 (14) (2011) 141906.
[82] T. Ezaz, H. Sehitoglu, H.J. Maier, Energetics of twinning in martensitic NiTi, Acta Mater. 59 (15) (2011) 5893–5904.